Assessing Typhoon Soulik-induced morphodynamics over the Mokpo coast region in South Korea based on a geospatial approach

Sang-Guk Yum[1], Moon-Soo Song[2], Manik Das Adhikari[3*]

[1] Department of Civil Engineering, Gangneung-Wonju National University, Gangneung, Gangwon-do 25457, South Korea; skyeom0401@gwnu.ac.kr
[2] Department of Safety & Disaster Prevention Engineering, Kyungwoon University, Gumi, Gyeongsangbuk-do 39160, South Korea; songms0722@ikw.ac.kr
[3] Department of Civil Engineering, Gangneung-Wonju National University, Gangneung, Gangwon-do 25457, South Korea; rsgis.manik@gmail.com

Correspondence to: Manik Das Adhikari (rsgis.manik@gmail.com)

Abstract

The inner shelf and coastal region of the Yellow Sea along the Korean peninsula are frequently impacted by Typhoons. The Mokpo coastal region in South Korea was significantly affected by typhoon Soulik in 2018, the deadliest typhoon strike to the southwestern coast since Maemi in 2003. Typhoon Soulik overran the region, causing extensive damage to the coast, shoreline, vegetation, and coastal geomorphology. Therefore, it is important to investigate its impact on the coastal ecology, landform, erosion/accretion, suspended sediment concentration (SSC) and associated coastal changes along the Mokpo region.

In this study, net shoreline movement (NSM), normalized difference vegetation index (NDVI), fractional vegetation coverage (FVC), coastal landform change model, normalized difference suspended sediment index (NDSSI), and SSC-reflectance relation have been used to analyze the coastal morphodynamics over the typhoon periods. We used pre-and post-typhoon Sentinel-2B MSI images for mapping and monitoring the typhoon effect. The findings highlighted the significant impacts of typhoons on coastal dynamics, wetland vegetation and sediment resuspension along the Mokpo coast. It has been observed that typhoon-induced SSC influences shoreline and coastal morphology. The outcome of this research may provide databases to manage coastal environments and a long-term plan to restore valuable coastal habitats. In addition, the findings may be useful for post-typhoon emergency response, coastal planners, and administrators involved in the long-term development of human life.

Keywords: Typhoon Soulik, Coastal changes, NDVI, FVC, Suspended sediment movement, Shoreline change, Mokpo Coast.

1. Introduction

Typhoons are one of the most destructive natural calamities. Strong winds that accompany typhoons during landfall damage the environment, coastline, wildlife, people, and public and private properties in coastal and inland areas (Shamsuzzoha et al., 2021; Xu et al., 2021; Mishra et al., 2021a; Nandi et al., 2020; Sadik et al., 2020; Sahoo and Bhaskaran, 2018; Hoque et al., 2016). Many coastal and near-coastal countries are plagued by typhoon-induced storms, flooding, deforestation, and increased soil salinity (Rodgers et al., 2009). Typhoons (tropical cyclones) have caused 1,942 disasters in the past 50 years, resulting in 779,324 fatalities and USD 1,407.6 billion in economic losses worldwide (WMO, 2020), demonstrating their effects on both the global and regional economies (Bhuiyan and Dutta, 2012; Mallick et al., 2017). The effects of typhoons include saltwater intrusion, soil fertility depletion, reduced agricultural productivity, life losses, coastline erosion, vegetation damage, and massive economic disasters (Mishra et al., 2021b).

According to instrumental data collected since 1904, typhoon intensity on the Korean peninsula has grown during the previous 100 years (Yu et al., 2018; Cha et al., 2021). A total of 188 typhoons, about three annually, have affected the coastal region from 1959 to 2018 (KMA, 2018). Among past Typhoons, RUSA (2002), MAEMI (2003), NARI (2007), and SOULIK (2018) heavily affected the southwestern coast, causing extensive damage to lives and properties (KMA, 2011; 2018). Furthermore, people living in these regions have faced serious coastal floods caused by these events for more than a half-century (Moon et al., 2003). Mokpo coastal region, located in the southwest coast of South Korea, has been hit by 58 typhoons since 1980, with most occurring in the July to October period (Kang et al., 2020; Lee et al., 2022). The rapid growth of coastal economies and populations in recent years has made these areas more susceptible to typhoon disasters. Therefore, the increasing frequency of typhoons on the southwestern coasts is a significant issue for disaster management.

Several studies (Halder and Bandyopadhyay, 2022; Wang et al., 2021; Shamsuzzoha et al., 2021; Kumar et al., 2021; Sadik et al., 2020; Konda et al., 2018; Parida et al., 2018; Zhang et al., 2013; Yin et al., 2013; Li and Li., 2013; Rodgers et al., 2009) have been carried out in South Asia using various techniques to map the hazard, vulnerability, risk and effects of typhoon disasters. Remote sensing and geospatial technology play a crucial role in monitoring a variety of natural disasters (Wang and Xu, 2018; Mishra et al., 2021b; Charrua et al., 2021). The majority of studies on typhoon-induced coastal dynamics rely on passive optical remote sensing and identify natural disaster damage using changes in landuse data, vegetation indices,

and geospatial techniques (Mishra et al., 2021a; Xu et al., 2021; Nandi et al., 2020). The post-typhoon damage assessment research in South Korea mostly focused on property loss, economic losses, and casualties (Yum et al., 2021; Kim et al., 2021; Hwang et al., 2020). However, the coastal morphodynamics along the Mokpo coast over the typhoon period have not been investigated in detail. Thus, this study's primary focus is to determine the effects of typhoon Soulik on coastal ecology, landforms, erosion/accretion, suspended sediment movement and associated coastal changes along the Mokpo coast.

The normalized difference vegetation index (NDVI) and variations in NDVI (ΔNDVI) have been used to map the extent of vegetation destruction and details on the degree of damage after the typhoon (Wang et al., 2010; Datta & Deb, 2012; Zhang et al., 2013; Kumar et al., 2021; Xu et al., 2021). Vegetation damage can be seen by the negative change in NDVI values between the post-and pre-typhoon period (Mishra et al., 2021a; Hu and Smith, 2018). On the other hand, fractional vegetation coverage (FVC) is a crucial quantitative indicator of the vegetation cover of the land surface (Zhang et al., 2021; Wang and Xu, 2018; Song et al., 2017). Therefore, FVC has also been used to assess the extent of vegetation damage caused by typhoon Soulik and to analyze its impact on vegetation cover. The coastline movement over the typhoon periods has been analyzed using the Digital Shoreline Analysis System (DSAS) program (Tsai, 2022; Adhikari et al., 2021; Bishop-Taylor et al., 2021; Santos et al., 2021). In order to monitor and protect coastal habitats, we need to understand the distribution and movement of SSC between rivers and coastal waters. Thus, the normalized difference suspended sediment index (NDSSI) (Kavan et al., 2022; Shahzad et al., 2018; Hossain et al., 2010) and the SSC-reflectance algorithm developed by Choi et al. (2014) for the Mokpo coastal region have been used to monitor SSC distribution. Furthermore, to understand the morphodynamics of the coastal landform due to the typhoon, a GSI-based coastal change model has been developed. Four coastal landform classes, i.e., tidally influenced land (wetland land, wetland vegetation) and non-tidally influenced land (land and water), have been used for the coastal morphodynamic analysis (Maiti and Bhattacharya, 2011). The change detection technique has been employed to quantify the pre and post-typhoon coastal changes. This approach focuses on details of morphological changes within the coast and highlights the minor changes caused by the typhoon.

This study uses Sentinel-2 MSI images as a primary data source to examine the morphodynamics and effects of Typhoon Soulik on coastal ecology. Accordingly, the objectives of this study are to (i) quantify and mapping of coastal landform dynamics prior to

102 and after the typhoon, (ii) examine shoreline movement and assess coastal erosion and
103 accretion, (iii) assess the degree of typhoon damage to vegetated land, and (iv) analyze changes
104 in SSC and the response of sediment dynamics over the typhoon period. Coastal managers can
105 use this study to develop and implement appropriate strategies and practices to protect natural
106 ecosystems and post-disaster rehabilitation.

107 **2. Study Area**

108 The Mokpo coast is located in the southwestern part of South Korea and is characterized by
109 muddy flats with wide tidal ranges (Choi et al., 2007; Kang et al., 2007), as depicted in Figure
110 1. The inner part of the coast includes harbor and industrial complexes, a large residential area,
111 and a wastewater treatment plant. Mokpo coast is most frequently hit by typhoons, which cause
112 the most significant amount of property damage and loss of human lives (Kang et al., 2020;
113 Lee, 2014). According to storm surge records, the Mokpo coastal region has experienced the
114 highest number of typhoons (58) since 1980 due to its geographical location (Lee et al., 2022;
115 Kang et al., 2020). The tidal range has been observed to be broader, with the extreme high tide
116 60cm higher and the extreme low tide 43cm lower in the Mokpo coast (Lee et al., 2022; Kwon
117 et al., 2018). This fluctuation resulted in significant flooding during the typhoon period. High
118 water and waves severely damage the coastal structures and environment, especially during
119 surges (Tsai et al., 2006). The Mokpo coastal region is characterized by a strong ebb dominant
120 pattern because of its complex bathymetry, scattered islands and extensive tidal flats (Byun et
121 al., 2004; Kang and Jun, 2003; Kang, 1999).

122 The vast tidal flat of the Mokpo coast serves as a habitat for many different species, has
123 a large production capacity, and is highly regarded for its role in cleaning up pollution and
124 controlling floods and typhoons (Lee et al., 2021; Na, 2004). Furthermore, the powerful storm
125 has affected the coastal wetlands (mudflats) that serve as the primary spawning and nursery
126 grounds for fish and other marine life. However, Choi (2014) observed that tidal flat systems
127 in the Korean peninsula are actively responding to various phenomena, such as tides, waves,
128 and typhoons. The wetland, coastal vegetation and coastline along the Mokpo coastal region
129 have been disturbed due to the extreme climatic events. It has been observed that most typhoon
130 passages severely impacted the tidal flat environment and caused morphodynamics along the
131 Mokpo coast.
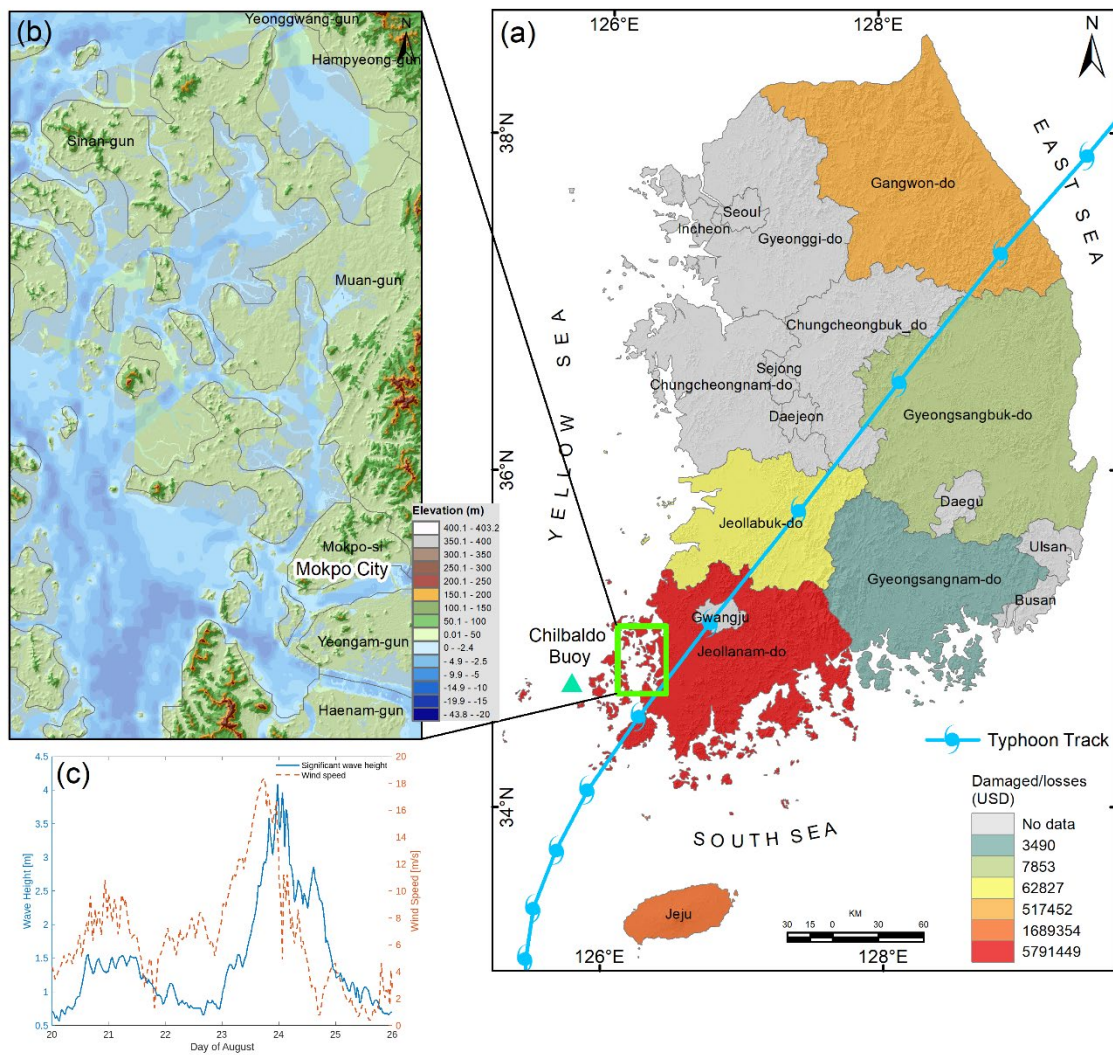
Figure 1. (a) Typhoon Soulik passage passed through the Mokpo coastal region on 23rd August 2018 (Typhon track data were downloaded from https://www.ncdc. noaa.gov/ibtracs/), while the background shades represent province-wise recorded damaged/loss distribution reported by Member Report (2018), (b) Topography variation of the Mokpo coastal region (elevation data acquired from NGII (2018), https://www.ngii.go.kr/, and bathymetry data downloaded from GMRT, https://www.gmrt.org), and (c) Variation of significant wave height and wind speed from August 20 to 25, 2018 recorded by Chilbaldo Buoy Station (located near the landfall area) during the typhoon Soulik (Data source: http://wink.kiost.ac.kr/map/map.do#).

2.1 Typhoon Soulik

The southwestern coast of the Korean peninsula was ravaged by the strong intensity typhoon Soulik, which hit the Mokpo coast on 23rd August 2018 (Ryang et al., 2021). On 16th August, it developed near Palau as a tropical depression. Subsequently, it strengthened into a tropical storm before intensifying into a typhoon (Lee et al., 2022). It moved into the East China

150 Sea on 20th August with a maximum intensity of 950 hPa (44 m/s) and lasted until 22nd August.
151 The Korea Meteorological Administration (KMA) issued typhoon warnings, and national and
152 local authorities took preventative measures to limit potential damage. On 23rd August, around
153 14 UTC, Typhoon Soulik made landfall close to Mokpo city, located on Korea's southwest
154 coast. The typhoon remained on the mainland for an additional 12 hours before moving to the
155 East Sea, where it underwent a transformation and became an extra-tropical cyclone. It had a
156 maximum sustained wind speed of 30.2 m/s observed at Gageodo in South Jeolla Province and
157 a central pressure of 975 hPa (Member Report, 2018). Meanwhile, the strongest gust was
158 observed at Mt. Halla, with a peak gust of 62 m/s. It also dumped tremendous rain (Kang and
159 Moon, 2022; Kang et al., 2020; Yu et al., 2018; Cha et al., 2021). The buoy station near Jeju
160 Island has recorded extreme sea surface conditions, including a maximum wave height of 15m,
161 gusts of 35 m/s, and a drop in water temperature of 10°C. (Kang et al., 2020; Yoon et al., 2021).
162 Figure 1(c) illustrates the variations in sea surface parameters between August 20 and August
163 25, 2018, in the vicinity of the landfall region (Chilbaldo buoy), including wind speed and
164 significant wave height. It was observed that a significant wave height, i.e., 4-6 m, was recorded
165 at Chilbaldo Buoy station. According to the Ministry of the Interior and Safety (MOIS),
166 typhoon Soulik caused various damages and disruptions across various regions in the country.
167 One woman was reported missing in the coastal area of Jeju, and three people sustained
168 injuries. A total of 362 facilities were damaged. In addition, the typhoon resulted in power
169 outages for 26,830 houses and flooding that affected over 3,063 hectares of farmland (Member
170 Report, 2018). Furthermore, the typhoon destroyed extensive vegetation with strong gusts and
171 damaged non-residential structures along the Mokpo coast. A province-wise breakdown of the
172 damage and losses caused by the typhoon is depicted in Figure 1(a). The total damage caused
173 by Typhoon Soulik in South Korea was $45 million (KMA, 2018).

174

175 **3. Data and Methods**
176 **3.1 Data Sources and pre-processing**
177 Typhoon-induced coastal dynamics along the Mokpo coast have been studied using the
178 pre-and post-event Sentinel-2 MSI images. A multispectral instrument (MSI), Sentinel-2,
179 consists of two polar-orbiting satellites, Sentinel-2A and Sentinel-2B, launched in June 2015
180 and March 2017, respectively (ESA, 2020). The Sentinel 2 MSI has a 290 km wide field of
181 view, a minimum revisits period of five days, 13 spectral bands ranging from visible to

shortwave infrared (SWIR), and spatial resolution of 10m (4 bands), 20m (6 bands), & 60m (3 bands) (ESA, 2020). The Sentinel-2 User Manual describes the MSI's radiometric, spectral, and spatial characteristics (ESA, 2020).

The cloud-free Sentinel-2 MSI level 1C satellite images with a relatively fine spatial resolution (10m) for the pre-and post-typhoon period have been downloaded from the Copernicus Scientific Data Hub (https://scihub.copernicus.eu/dhus/) as depicted in Figure 2. Level 1C is a 12-bit radiometric product that was presented the top of the atmospheric reflectance value (Phiri et al., 2021). The open-source software SNAP (Sentinel Application Platform) has been used to process the Sentinel-2 MSI images such as masking, band visualization, atmospheric correction etc. We used SANP's iCOR tool (image correction for atmospheric effect) for atmospheric correction of the Sentinel 2 MSI data over the land and water (Tian et al., 2020; Keukelaere et al., 2018). After that, satellite remote sensing reflectance (R_r) images were used to monitor the coastal dynamics in the Mokpo coastal region over the typhoon period.
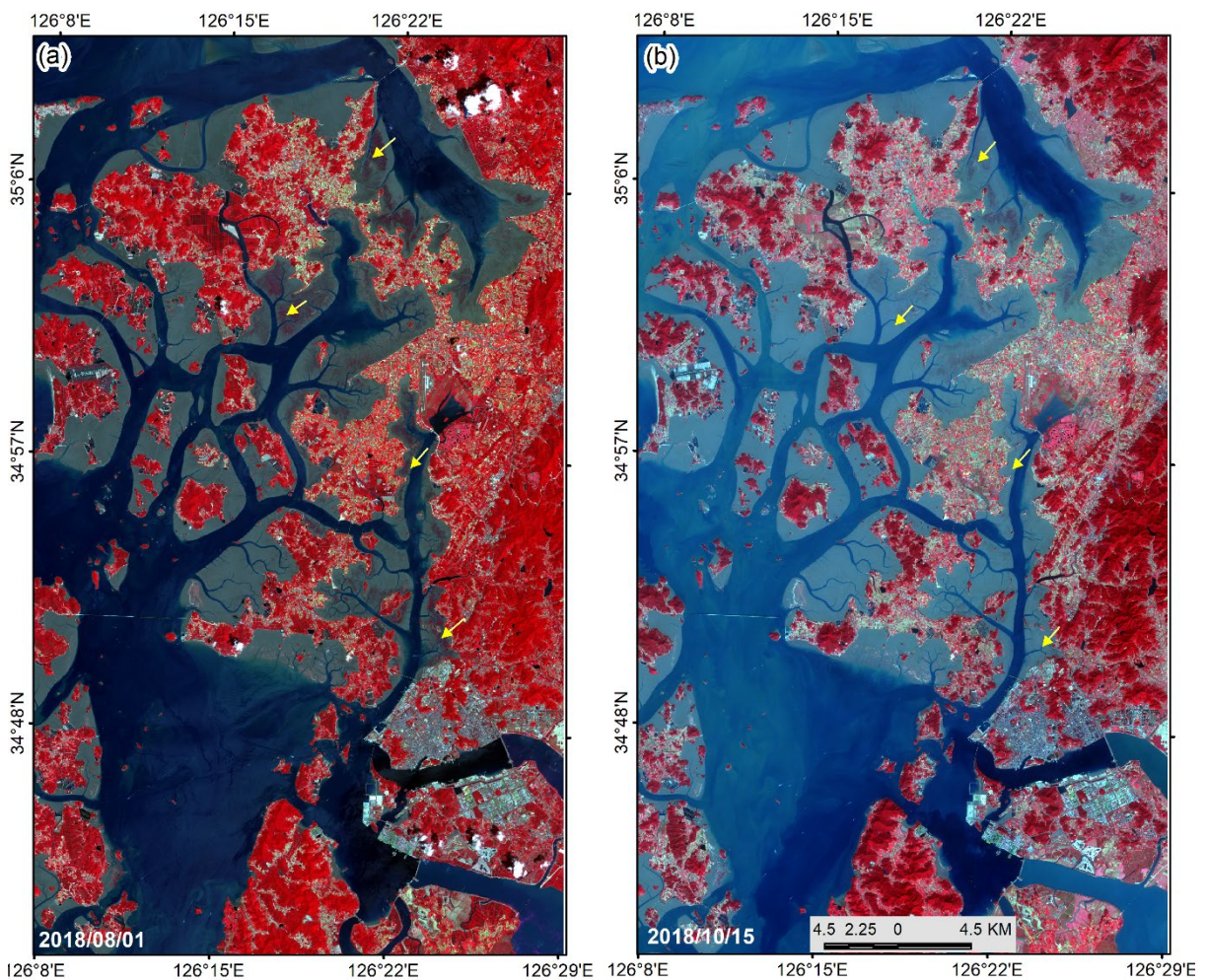
Figure 2: Pre (a) and post-typhoon (b) standard false color composite of reflectance image of

the Mokpo coastal region (Sentinel-2 MSI level 1C satellite images are downloaded from https://scihub.copernicus.eu/dhus/). The arrows indicate extensive vegetation damage due to typhoon Soulik.

On the other hand, to exclude the impact of tidal changes, satellite images have been chosen during low tide conditions (Maiti and Bhattacharya, 2009). The tide height has been computed using the WXTide32 program (Hopper, 2004). Several researchers have discussed the significance of low tide satellite data for coastal mapping and dynamics modeling (Nayak, 2002). The details of pre- and post-typhoon satellite data used in the study are listed in Table 1. In addition, the coastal morphology was also investigated using high-resolution (5m×5m) topography data (i.e., LiDER DEM) provided by the Korean National Geographic Information Institute (NGII) and bathymetry data obtained from GMRT (https://www.gmrt.org) (Fig. 1b).

Table 1. The details of Sentinel-2 MSI data used for coastal dynamic modeling.

Periods	Date of acquisition	Sensor	Cloud cover (%)	Tidal Height (m)
Pre-typhoon	2018/08/01	Sentinel-2B MSI	1.3464	0.77
Post-typhoon	2018/10/15	Sentinel-2B MSI	0.6548	1.01
	2019/10/20	Sentinel-2B MSI	2.8444	1.02

3.2. Typhoon-induced coastal dynamic modeling

This study aims to analyze the typhoon Soulik-induced coastal dynamics and associated coastal changes along the Mokpo coastal region. Figure 3 depicts an integrated flowchart of the impact of a typhoon on a coastal system. The outline of the study is divided into four sections: (a) coastal vegetation disturbance mapping, (b) coastal landform mapping and change analysis, (c) suspended sediment concentration variation modeling, and (d) coastal erosion and accretion analysis. The details methodology of each objective has been discussed in the subsequent section.
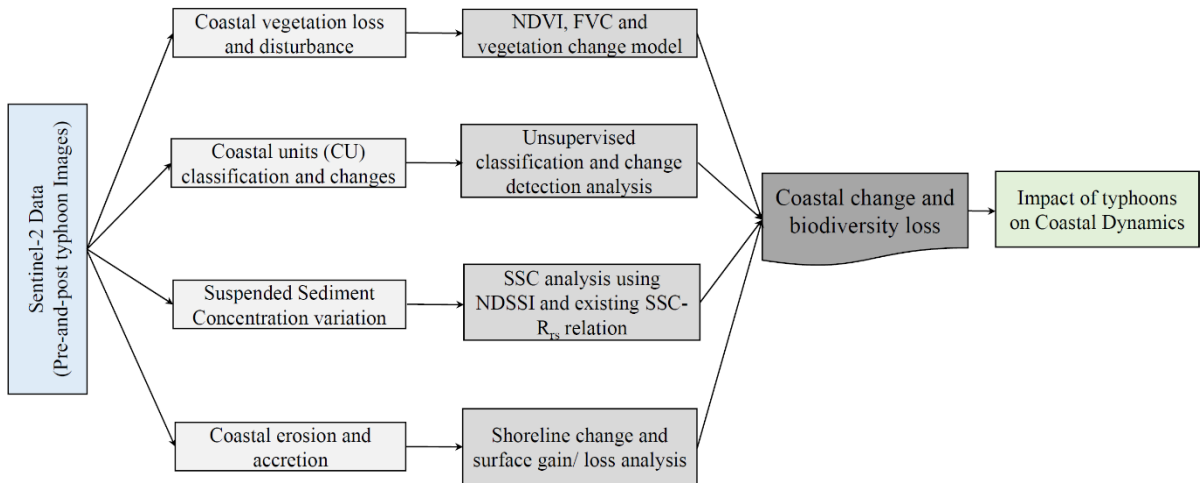
220

221 Figure 3. Geospatial-based approach for coastal dynamics due to a typhoon.

3.2.1 Analyses of coastal vegetation loss and disturbance

223   Vegetation damage severity mapping (VDSM) has been performed using pre-and post-
224 event satellite images. NDVI and FVC are widely used techniques for measuring vegetation
225 density, health status, regional vegetation condition, and detecting vegetation disturbances (Xu
226 et al., 2021; Mishra et al., 2021b; Wang et al., 2010; Yang et al., 2018, Wang and Xu, 2018;
227 Carlson and Ripley, 1997). Subsequently, numerous studies (Xu et al., 2021; Mishra et al.,
228 2021a; Charrua et al., 2021; Shamsuzzoha et al., 2021; Kumar et al., 2021; Nandi et al., 2020;
229 Wang and Xu, 2018; Konda et al., 2018; Zhang et al., 2013; Rodgers et al., 2009) have shown
230 that the NDVI and FVC is a reliable indicator of post-typhoon damage detection. Therefore, in
231 this study, the vegetation damage due to typhoon Soulik has been determined using the NDVI
232 and FVC approach. The NDVI has been calculated by using the following Eq. (1) (Rouse et
233 al., 1974; Filgueiras et al., 2019):

234 $NDVI = \dfrac{\rho\text{NIR}-\rho\text{RED}}{\rho\text{NIR}+\rho\text{RED}}$ (1)

235 where ρNIR and ρRED are the spectral reflectances corresponding to the eighth (832.8–
236 832.9nm) and fourth (664.6– 664.9nm) Sentinel-2 MSI bands, respectively (Xu et al., 2021).
237 In general, NDVI values range from -1.0 to 1.0; the higher the NDVI value, the better the
238 conditions for vegetation development, and extremely low values indicate the presence of
239 water. Furthermore, the NDVI value above 0.4 indicates vegetated surfaces, and those between
240 0.25 and 0.40 signify soils with the presence of vegetation (Charrua et al., 2021). The vigor of
241 the vegetation increases as the NDVI values come closer to 1.00 (Rouse et al., 1974). Numerous
242 studies have established the NDVI threshold for vegetated land (e.g., Xu et al., 2021; Wong et

al., 2019; Liu et al., 2015; Eastman et al., 2013; Yang et al., 2012; Sobrino et al., 2004). Most researchers noted that the NDVI threshold value for vegetation cover typically ranges from 0.15-2.0 (Xu et al., 2021; Eastman et al., 2013; Sobrino et al., 2004). Therefore, the vegetated pixels (e.g., NDVI threshold > 0.20) present in pre and post-typhoon NDVI images have been used for vegetation severity analysis. The NDVI threshold is considered to reduce the influence of land cover change from the pre-typhoon (2018-08-01) to post-typhoon (2018-10-15) periods.

The degree of vegetation damage has been determined by comparing the NDVI values of the pre-and post-typhoon periods. Various researchers have frequently used the direct difference of NDVI to determine the damage severity caused by typhoons to naturally vegetated land (Wang and Xu, 2018; Konda et al., 2018). It has been calculated on a cell-by-cell basis by subtracting the pre-typhoon NDVI image from that of the post-typhoon in ArcGIS software using map algebra (Zhang et al., 2013; Cakir et al., 2006). The following equation is used to calculate the ΔNDVI (Wang and Xu, 2018),

$$\Delta NDVI = NDVI_{post-typhoon} - NDVI_{pre-typhoon} \tag{2}$$

The difference in NDVI (i.e., ΔNDVI) illustrates the change in natural vegetation, while a negative ΔNDVI value indicates the damage inflicted by a typhoon to the vegetation cover (Xu et al., 2021).

The relative change in NDVI value has been used to investigate the geo-ecological impact on the forest area (Mishra et al., 2021b). The relative vegetation changes ($NDVI_r$) after Soulik have been determined by using the following Eq. (3) (Kumar et al., 2021),

$$NDVI_r = \frac{\Delta NDVI}{NDVI_{pre-typhoon}} \times 100 \tag{3}$$

where the negative $NDVI_r$ value indicates vegetation loss caused by typhoons, and the positive $NDVI_r$ value shows vegetation gain. The $NDVI_r$ value has been classified into three categories corresponding to pixels with decreased, no change, or increased vegetation cover.

On the other hand, we analyze FVC in conjunction with NDVI, which provide additional insights into vegetation conditions and damage severity. Numerous researchers (Wang and Xu, 2018; Song et al., 2017; Bao et al., 2017; Chu et al., 2016; Amiri et al., 2009) used FVC to analyze vegetation damage, restoration, recovery, inter-annual variability. It is calculated as the ratio of the area covered by vegetation to the total area of the landscape. It is expressed as a percentage and can range from 0 to 100%. In the present study, FVC was

274 calculated before and after the typhoon using the derived NDVI data (Wang and Xu, 2018).

275 The formula of FVC is as follows (Wang and Xu, 2018; Amiri et al., 2009; Carlson and Ripley,

276 1997),

277 $$FVC = [(NDVI - NDVI_m)/(NDVI_{max} - NDVI_m)]^2 \qquad (4)$$

278 where, $NDVI_m$ and $NDVI_{max}$ represent the $NDVI_{min}$ and $NDVI_{max}$ values calculated using

279 equation (1) (Zhang et al., 2021; Ge et al., 2018). The calculated FVC values vary between 0

280 and 1. After that, the FVC values were converted to percentages to fit the actual FVC

281 classification scheme (Wang and Xu, 2018), which consists of five classes: low (0-20%),

282 medium-low (20-40%), medium (40-60%), medium-high (60-80%), and high (80-100%).

283 Further, the difference in FVC values between the pre-and post-typhoon images was used to

284 calculate the extent of vegetation damage using the following equation,

285 $$\Delta FVC = FVC_{post-typhoon} - FVC_{pre-typhoon} \qquad (5)$$

286 where, ΔFVC is the difference value between the FVC before and after the typhoon. The ΔFVC

287 value represents alterations in vegetation conditions and damage intensity, while a negative

288 value of ΔFVC indicates the extent of damage caused by a typhoon to vegetation cover (Wang

289 and Xu, 2018).

290

291 **3.2.2 Coastal landform classification and change analysis**

292 Typhoons have adversely affected the coastal landform and ecology of the south and

293 west coasts of the Korean peninsula every year. Therefore, a GSI-based coastal change model

294 has been developed to understand the morphodynamics of coastal landforms during typhoons.

295 In the present study, we considered four coastal landform classes, i.e., wetland, wetland

296 vegetation, land, and water, for the coastal morphodynamic analysis (Maiti and Bhattacharya,

297 2011). The method consists of two algorithms, i.e., (a) the ISODATA algorithm used to classify

298 the coastal landform with four main classes, i.e., water, wetland, wetland vegetation, and land,

299 and (b) the change detection technique used to quantify the pre- and post-typhoon coastal

300 changes. In this approach, we accentuate in-depth morphological changes and emphasize minor

301 changes along the Mokpo coast caused by typhoon Soulik.

302 The pre-and post-typhoon Sentinel-MSI images have been classified using the

303 unsupervised classification technique to distinguish among different coastal landforms of the

304 study region. This approach is used to determine which types of coastal landforms were

305 adversely affected by Typhoon Soulik and which of them have recovered more quickly than

306 others. ERDAS Image software has been used to run the unsupervised classification algorithm

307 (ERDAS, 1997). Based on the k-means algorithm, this technique reduces variability within
308 pixel clusters (Charrua et al., 2021; Aswatha et al., 2020; Bhowmik et al., 2013). Finally, pre-
309 and post-typhoon Sentinel-2 MSI images have been classified into four coastal landform
310 classes: land, water, wetland, and wetland vegetation.

311   The accuracy assessment is a commonly used method to determine how closely the
312 classified map matches the reference data (Congalton, 1991). In the present study, the classified
313 data (i.e., coastal landforms maps) have been derived through an unsupervised classification
314 technique, while 550 random samples collected from different parts of the Sentinel- 2MSI
315 standard false-color image are considered reference data. Thereafter, a confusion matrix was
316 developed based on the reference and classified data to evaluate accuracy statistics (Story and
317 Congalton, 1986). The *kappa* coefficient (*k*) has been used to determine the quantitative
318 accuracy of the classified map (Landis and Koch, 1977). The assessment is quantified using
319 three different statistics: overall accuracy, producer accuracy, and user accuracy (Story and
320 Congalton, 1986). The model's precision is classified into five categories based on the *k* values:
321 near perfect ($k > 0.8$), substantial ($0.6 < k < 0.8$), moderate ($0.4 < k < 0.6$), fire ($0.2 < k < 0.4$),
322 and poor ($k < 0.2$) (Landis and Koch, 1977).

323   The land transformation model based on mutual spatial replacements has been applied
324 during the post-classification stage, as shown in Figure 4. The classified coastal landform
325 classes, such as land, wetland, wetland vegetation, and water, have been spatially replaced in
326 order to create coastal-change units. For example, the coastal landform class of wetland
327 vegetation in the pre-typhoon period replaced by water in the post-typhoon period indicates the
328 change class of wetland vegetation replaced by water. A total of nine coastal-change classes
329 have been derived, as illustrated in Figure 4(b).
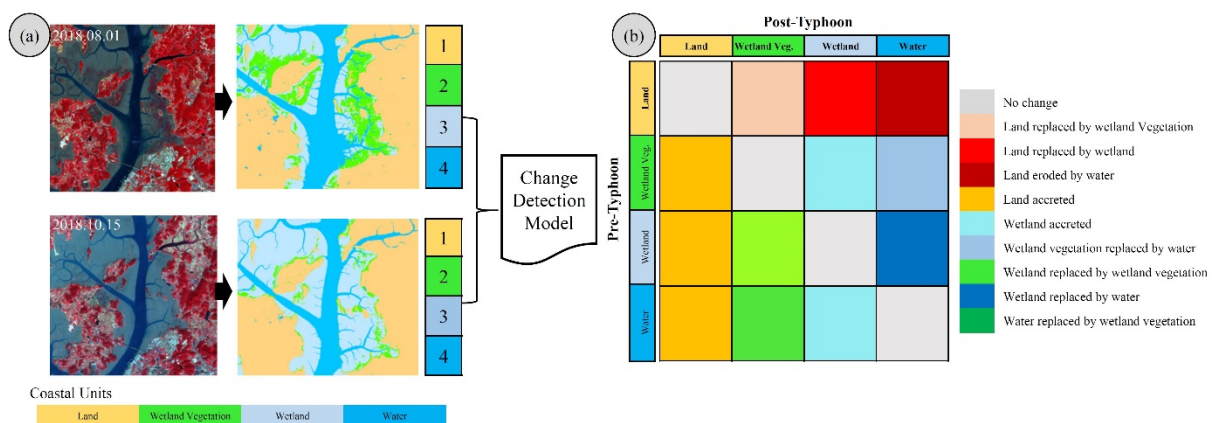
331 Figure 4. The coastal-change model exhibits spatial replacements among coastal landform
332   classes.

333

3.2.3 Suspended sediment concentration modeling

The suspended sediment concentration (SSC) distribution in coastal regions is a significant indicator of changes in the marine environment caused by typhoon-induced storm surges, strong waves, and subsequent coastal flooding (Min et al., 2012; Gong and Shen, 2009). In a short period, a typhoon may drastically influence the water column structures (Souza et al., 2001), change the transport and deposition of sediment (Li et al., 2015), and affect the distribution of nutrients and biological production in the affected seas (Wang et al., 2016). Extreme storms or typhoons can modify suspended sediment distribution in coastal areas, which can significantly change marine habitats (Chau et al., 2021; Lu et al., 2018; Li land Li, 2016). Due to strong typhoon wind stress, the concentration of suspended particles in the seawater column and sediment resuspension may increase dozens of times before and after the event (Lu et al., 2018; Bian et al., 2017). Thus, typhoons significantly affect suspended sediment movement in the coastal region (Zhang et al., 2022; Li and Li, 2016; Goff et al., 2010). The spatiotemporal distribution of SSC can be impacted by variations in tidal phase, runoff, and wind speed (Tang et al., 2021). Furthermore, the resuspension of sediment can cause numerous problems in ocean engineering and change the region's ecology (Kim, 2010). The amount of material delivered to and adverted across the shelf by typhoons is considerably larger than that of winter storm systems (Dail et al., 2007). The southern and western part of the Korean peninsula is affected by an average of three typhoons annually passing through the Yellow Sea (KMA, 2018; Altman et al., 2013). Some studies on SSC distribution impacted by artificial construction along the coastal region of the Yellow Sea have been undertaken by several researchers (i.e., Lee et al., 2020; Eom et al., 2017; Min et al., 2012, 2014; Choi et al., 2014). However, the effects of typhoons on the sedimentary environment in the Mokpo coastal region have not yet been investigated. Therefore, it is imperative to carry out regional-scale SSC mapping and coastal modifications to reveal changes in the marine environment and sediment transport mechanisms over the typhoon period.

Remote sensing has long contributed to the advancement of water quality studies (Hossain et al., 2021). In the present study, we attempted to calculate both the qualitative and quantitative SSC in the inner-shelf region of the Mokpo coast using Sentinel-2B MSI data. The relative suspended sediment concentration has been calculated from pre- and post-typhoon Sentinel-2B MSI images using the NDSSI. NDSSI has been used in various water quality research (Kavan et al., 2022; Hossain et al., 2010). Further, many studies (Shahzad et al., 2018;

366 Arisanty & Saputra, 2017) have successfully used Landsat and Sentinel-2 data to calculate
367 NDSSI. This index determines the relative concentration of suspended sediment, with values
368 ranging from -1 to 1, where -1 indicates the highest concentration and +1 indicates the lowest
369 (Hossain et al. 2010). The NDSSI has been calculated by using Eq. (6).

370 $$NDSSI = \frac{\rho\text{Blue} - \rho\text{NIR}}{\rho\text{Blue} + \rho\text{NIR}} \quad\quad\quad\quad\quad\quad (6)$$

371 where ρBlue and ρNIR represent the surface reflectances of Band 2 (492.1– 492.4 nm) and
372 Band 8 (832.8 – 833.0 nm) of Sentinel-2 MSI data, respectively. The NDSSI is based on the
373 observation that turbid waters reflect more in the NIR band but less in the visible band. The
374 negative NDSSI value represents that the reflectance of water in the NIR band is greater than
375 that in the blue band (Shahzad et al., 2018; Hossain et al., 2010). Therefore, the positive values
376 of NDSSI represent lower SSC or more transparent water, while a negative value indicates
377 higher SSC. The spatial patterns of relative SSC during the typhoon period have been
378 determined using the NDSSI.

379 On the other hand, the empirical model has also been used to quantify the suspended
380 sediment concentration before and after typhoon Soulik. This method is widely used for SSC
381 mapping and monitoring around the world (Eom et al., 2017; Hwang et al., 2016; Son et al.,
382 2014; Min et al., 2012; Lee et al., 2011; Choi et al., 2014). For this purpose, we reviewed the
383 existing relations between the in-situ SSC (SSC, g/m^3) and remote sensing reflectance (R$_r$)
384 developed by various researchers for the southern and western coasts of South Korea, as
385 illustrated in Table 2. In the present study, the SSC algorithm developed by Choi et al. (2014)
386 for the Mokpo coastal region based on the in-situ SSC and a spectral ratio of water reflectance
387 around 660nm has been used to quantify the SSC distribution. The atmospheric corrected
388 sentinel-2 MSI image (Red band) has been used to calculate the SSC.

389

390 Table 2. Relationship between the remote sensing reflectance (R$_r$) and suspended sediment
391 concentration (SS, g/m^3).

Authors	Relation	Region	Wavelength (nm)
Min et al. (2012) Min et al. (2006)	Y=0.24e$^{188.3x}$	Saemangeum coastal area	560nm
Choi et al. (2014)	Y=1.545e$^{179.53x}$	Mokpo coastal, Gyeonggi Bay	660nm
Lee et al. (2011)	Y=16.2064e$^{15.3529x}$	Gwangyang Bay and Yeosu Bay	565nm
Choi et al. (2012) Lee et al. (2020)	Y=1.7532e$^{204.26x}$	Yellow Sea	660nm
Eom et al. (2017)	Y=1.5119e$^{179.85x}$	Nakdong River	660nm

Min et al. (2004)	$Y=0.99e^{199.9x}$	Saemangeum	560nm

3.2.4 Coastal erosion and accretion analysis

The shorelines (i.e., land and water boundary) of the Mopko coast for pre- and post-typhoon periods have been extracted using a semi-automatic technique (Maiti and Bhattacharya, 2009). Here, we used the normalized difference water index (NDWI) and manual digitization approach to separate the land and water boundary. The technique is widely used for dividing land and water boundary (Santos et al., 2021; Dai et al., 2019). By using Sentinel-2 imagery, NDWI can be achieved with the following formula (McFeeters, 1996),

$$NDWI = \frac{\rho\text{Green} - \rho\text{NIR}}{\rho\text{Green} + \rho\text{NIR}} \tag{7}$$

where ρGreen is the green band, and ρNIR is the near-infrared band of Sentinel-2 MSI data.

The extracted land and water boundary of the Mokpo region are then converted into polygons, and the shoreline has been determined using ArcGIS software. The shoreline change statistics have been calculated using the DSAS program (Thieler et al., 2009). The extracted shoreline for pre-and post-typhoon periods has been merged, and a 10m interval transect perpendicular to a baseline has been created (Santos et al., 2021). Thereafter, the NSM method was used to calculate the total shoreline movement (in meters) between the pre-and post-typhoon shoreline positions of each transect (Kermani et al., 2016).

$$NSM = sh_{post} - sh_{pre} \tag{8}$$

where sh_{post} and sh_{pre} represent the post and pre-typhoon shoreline positions, respectively.

On the other hand, the back-shore surface area changes due to shoreline movement (retreat/advance) over the typhoon period has also been calculated using the geo-statistical analyst tool. Several researchers (Awad and El-Sayed, 2021; Deabes, 2017; Karmani et al., 2016) have also previously mapped the surface changes of the backshore region. In order to produce the surface area-change map, we generated two polygons, one for each shoreline and then subtracted them from each other over the typhoon period using the Symmetrical Difference tool in ArcGIS software. Finally, two feature classes have been derived, one for erosion and another for accretion. In addition, the attribute table contained in each zone illustrates the magnitude of spatial changes (amounts of erosion and accretion) during the typhoon period.

4. Result and Discussion

4.1 Vegetation damage severity mapping (VDSM) before and after typhoon

4.1.1 VDSM based on the NDVI and FVC analysis

The VDSM shows the degree of vegetation damage due to typhoons. The comparison of pre-and post-typhoon NDVI and FVC distribution shows a significant loss of vegetated land as the number of no-productivity and low-productivity pixels increases in the post-typhoon NDVI and FVC image.

Figure 5 depicts the spatial distribution of pre and post-typhoon NDVI images. Further, to determine the severity of vegetation damage, the pre-and post-typhoon NDVI image has been classified into six categories, namely non-vegetation (-1.0-0.0), low-vegetation (0.0-0.2), medium-low vegetation (0.2-0.4), medium vegetation (0.4-0.6), medium-high vegetation (0.6-0.8) and high vegetation (0.8-1.0). The pre and post-typhoon mean NDVI values were observed to be 0.159 and 0.143, respectively, indicating a mean NDVI value decline of 0.016 after the typhoon.

NDVI

<0 [Non-vegetation]   0 - 0.2 [Low]   0.2 - 0.4 [Medium-low]   0.4 - 0.6 [Medium]   0.6 - 0.8 [Medium-high]   >0.8 [High-vegetation]
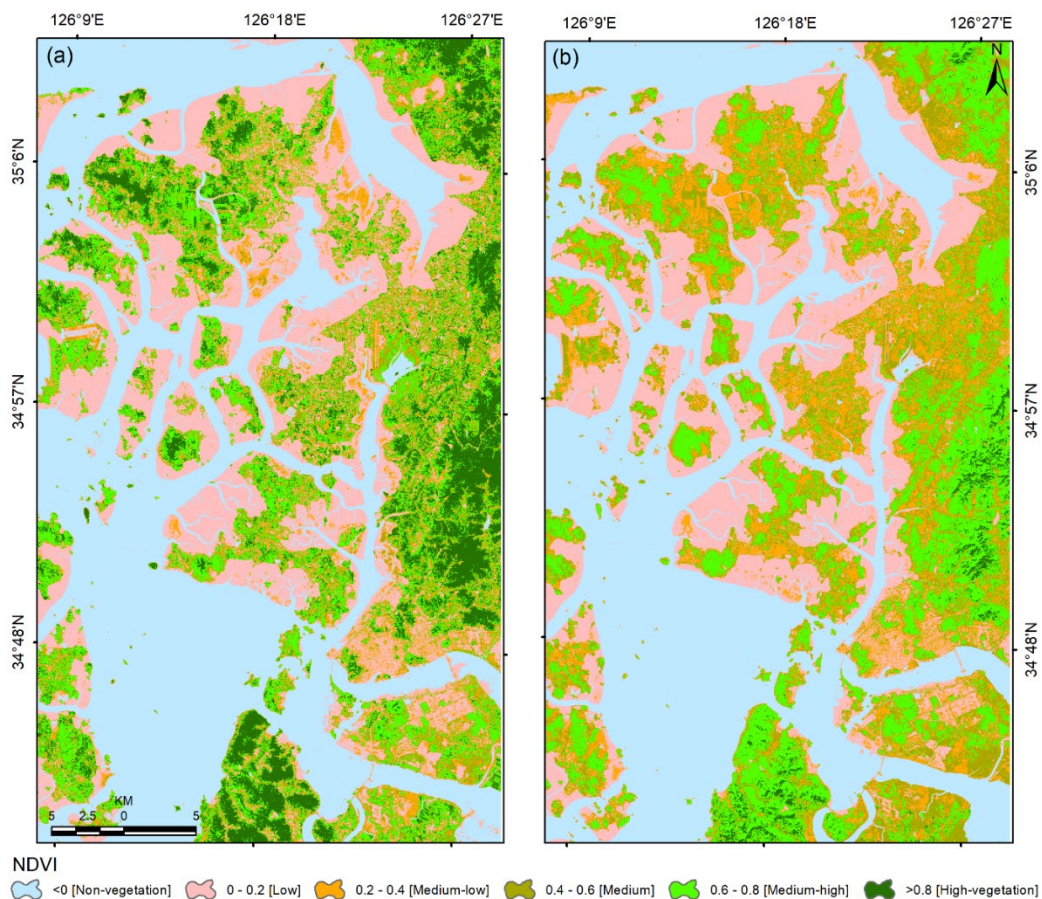
Figure 5. Status of vegetation greenness based on the NDVI data for the (a) pre-Soulik (01st August 2018) and post-Soulik (15th October 2018) period.

Table 3 depicts the area changes for each NDVI category over the typhoon period. It

441 has been observed that the high NDVI values (>0.8) have changed drastically after typhoon-
442 Soulik. The area changes in the low and non-vegetation categories along the Mokpo coastal
443 region revealed that the wetland (mudflat) had accreted after the typhoon. On the other hand,
444 the post-typhoon image was acquired two months after typhoon Soulik, which suggests that
445 the grasses and crops have recovered well. This recovery is reflected in Table 3 from medium-
446 low to medium-high NDVI levels.

447

448 Table 3. NDVI distribution over the study area before and after the typhoon.

NDVI levels	Pre-typhoon (km^2)	Post-typhoon (km^2)	Change (km^2)
Non-vegetation (-1 to 0)	673.7	647.6	-26.2
Low (0 to 0.2)	430.4	415.2	-15.2
Medium-low (0.2 to 0.4)	141.6	243.3	101.6
Medium (0.4 to 0.6)	132.5	225.3	92.8
Medium-high (0.6 to 0.8)	283.7	294.4	10.7
High (0.8 to 1.0)	183.6	19.8	-163.8

449

450 On the other hand, the physical presence of vegetation has also been measured using
451 FVC analysis. In general, NDVI provides information on the health and productivity of
452 vegetation, while FVC provides information on the physical presence and distribution of
453 vegetation. Figure 6 depicts the pre- and post-typhoon FVC map of the Mopko coast. The area
454 of each FVC category is illustrated in Table 4. The results reveal that the typhoon caused a
455 substantial decrease in FVC in the area, with the average FVC reducing significantly from
456 33.43% to 23.64% after the typhoon. It was observed that the medium-high to high FVC area
457 decreased from 485.4 km^2 to 211.9 km^2, while the medium-to-low FVC area increased from
458 1359.8 km^2 to 1633.3 km^2. The high FVC vegetation category was more severely affected and
459 decreased considerably after the typhoon. These results indicate that the typhoon significantly
460 impacted the wetland vegetation in the region.

461
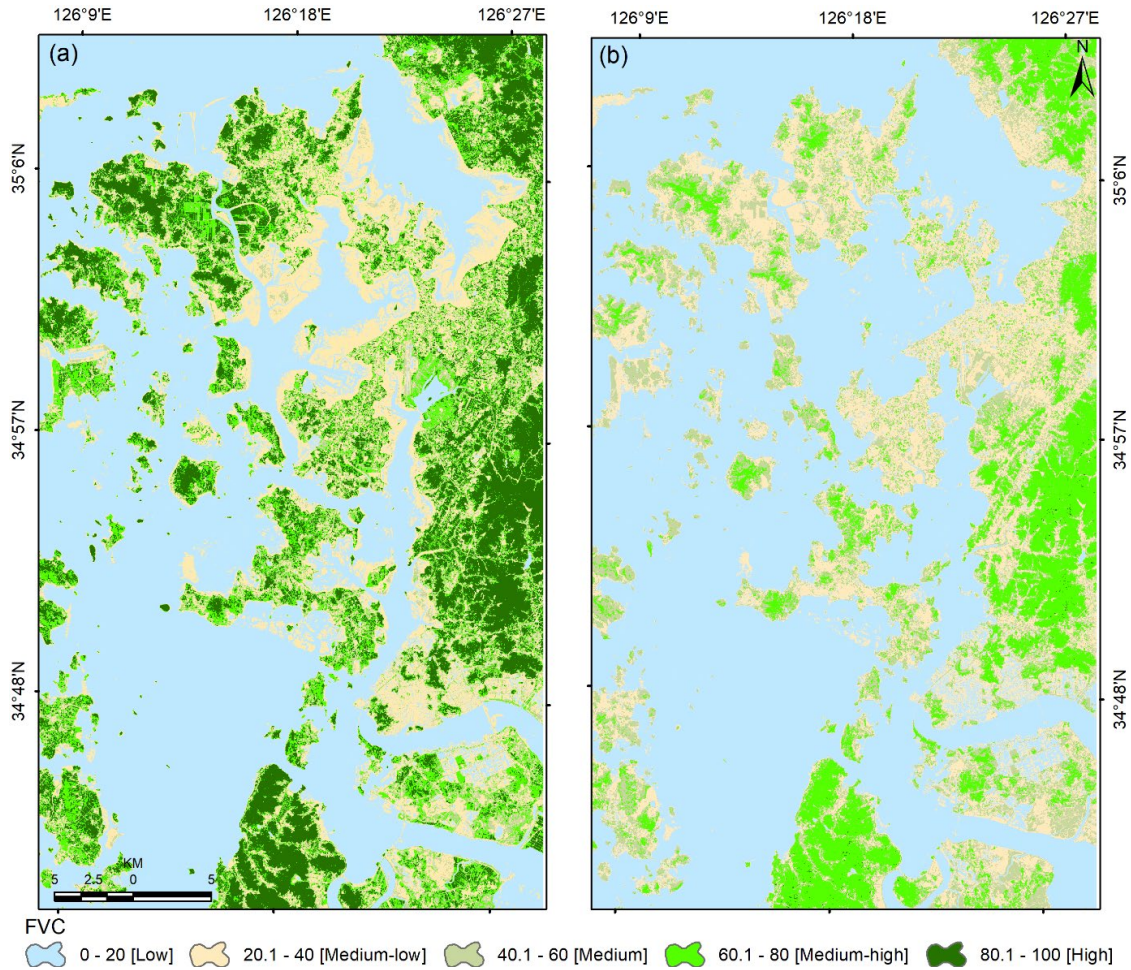
Figure 6. Status of vegetation based on the FVC analysis for the (a) pre-Soulik (01st August
2018) and post-Soulik (15th October 2018) period.

Table 4. Summary of FVC classes before and after the typhoon.

FVC levels (%)	Pre-typhoon (km^2)	Post-typhoon (km^2)	Change (km^2)
Non-vegetation (<20)	890.3	1053.3	162.943
Medium-low (20-40)	327.4	319.6	-7.811
Medium (40-60)	142.4	260.6	118.205
Medium-high (60-80)	206.1	211.5	5.365
High (80-100)	279.4	0.7	-278.671

In order to determine the damaged vegetation areas along the Mokpo coast, we compared pre-and post-typhoon NDVI images. A decrease in ΔNDVI is one of the most distinctive features of abrupt canopy modifications detectable by optical remote sensing (Xu et al., 2021). Thus, we can only determine vegetation deterioration from the two NDVI images. Subsequently, an NDVI threshold of 0.2 has been used to extract only vegetation features from the pre-and post-typhoon NDVI images. The threshold value has been manually adjusted to

473   achieve the highest accuracy of vegetation pixels. The extracted vegetated pixels have been

474   compared with reference samples randomly collected from the original high spatial resolution

475   images to determine the accuracy (Schneider, 2012; Xu et al., 2021). The two extracted

476   vegetation images obtained within six or seven weeks of typhoon Soulik's (i.e., before the

477   damaged vegetation had recovered) exhibits an overall accuracy of 95.7 % for pre-typhoon and

478   94.5% for the post-typhoon period.

479   Figure 7(a) depicts the spatial distribution of ΔNDVI, where the highest ΔNDVI

480   indicates a region with highly impacted vegetation areas. The negative ΔNDVI is attributed to

481   about 26.7% of the total area (1845.60 km^2), which suggests that Typhoon Soulik affected

482   approximately 493.98 km^2 of vegetated land. The lowest ΔNDVI value is -0.89, which

483   indicates either tree wind throws or a change in land surface cover from vegetation to build-up

484   land or other non-vegetation covers (Zhang et al., 2013). The results showed that wetland

485   vegetation and agricultural land experienced the most significant NDVI changes, with ΔNDVI

486   values below-0.3. This suggests that these two types of land cover were severely affected by

487   typhoon Soulik.

488   On the other hand, Figure 7(b) represents the change map derived from the ΔFVC,

489   which also indicates changed vegetation areas after the typhoon. The negative ΔFVC is

490   attributed to about 32.07% of the total area, which suggests that Typhoon Soulik affected

491   approximately 591.89 km^2 of vegetated land. It has also been observed that the pure vegetation

492   pixels (i.e., NDVI>0.6 and FVC>60%) were drastically changed over the typhoon period. The

493   changed area determined for NDVI and FVC is -153.43 km^2 and -273.40 km^2, respectively

494   (Tables 3 & 4). The results obtained from both techniques indicate a significant decrease in

495   vegetation cover after the typhoon. The probable reason for the change is that Typhoon Soulik

496   made landfall close to Mokpo coastal region.
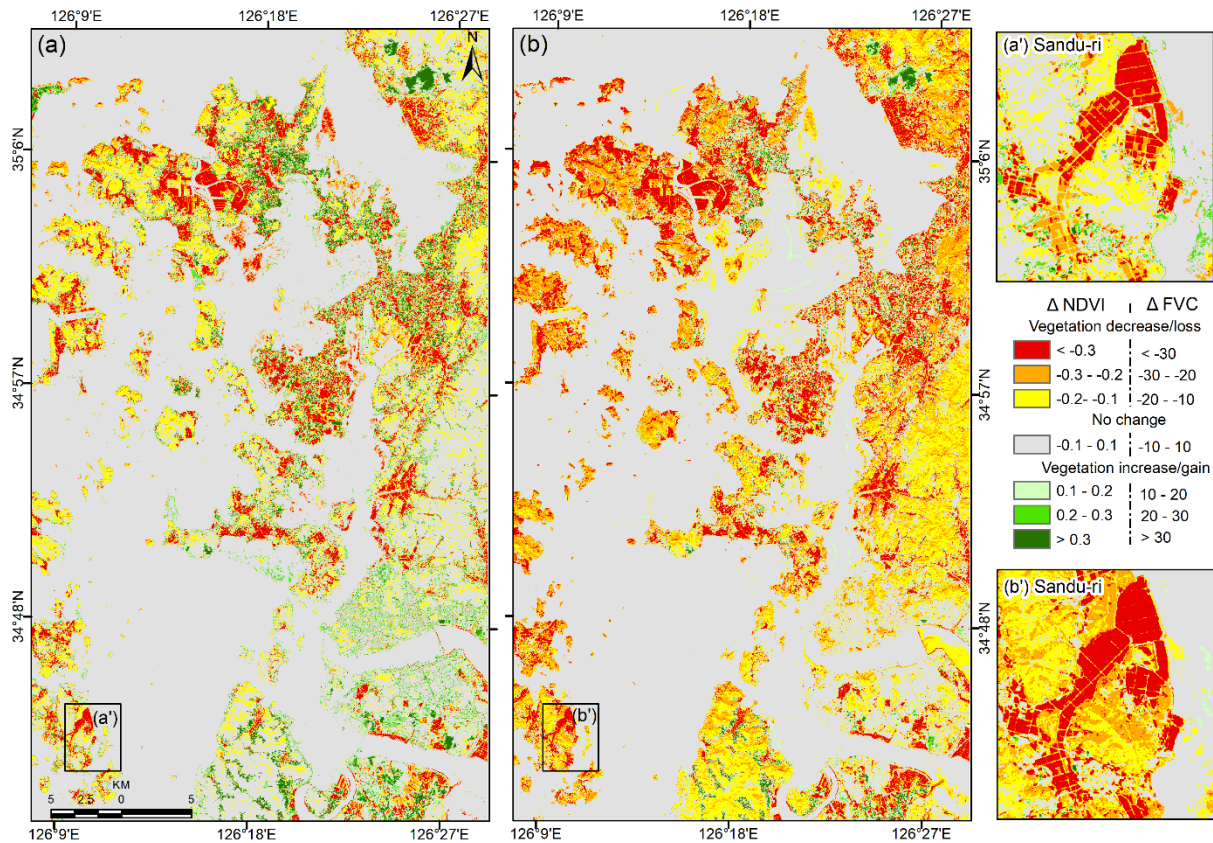
497

498 Figure 7. Vegetation change map of the Mokpo coastal region derived through two different
499 methods: (a) ΔNDVI and (b) ΔFVC, whereas zoom boxes show the vegetation
500 damage of Sandu-ri areas.
501

502 Figure 8 compares vegetation damage based on the number and percentage of the

503 decreased pixel of ΔNDVI and Δ FVC. It exhibits decreased pixels in different categories of

504 vegetation damage, ranging from low damage to extensive damage. The pixels showing the

505 most significant vegetation damage (i.e., ΔNDVI -0.2 to -0.5 and ΔFVC -20 to -50%) account

506 for about 30.9% and 61.5% of the total pixels, respectively. On the other hand, the pixels

507 showing extensive vegetation damage (i.e., ΔNDVI<-0.5 and ΔFVC<-50%) account for only

508 8.31% and 10.76% of the total pixels. It was observed that the dominant vegetation in the region

509 is wetland vegetation, which is mainly due to the prevalence of wetlands or mudflats in the

510 area. Therefore, the significant vegetation damage implies that wetland vegetation was most

511 severely impacted during typhoons.
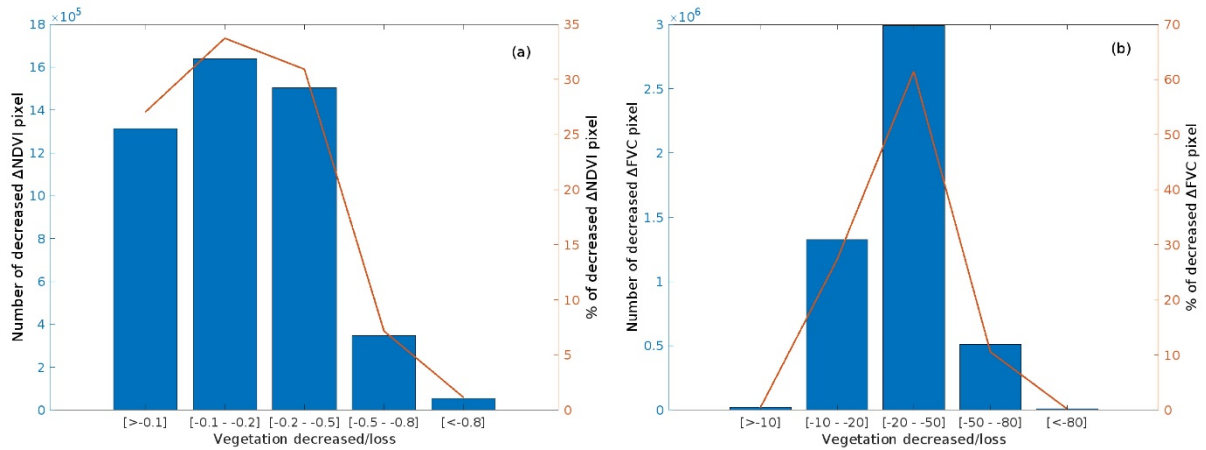
512

513 Figure 8. Comparison of vegetation damaged represented based on the number and percentage
514   of decreased pixels of (a) ΔNDVI and (b) Δ FVC.

515

516   The pre-and post-typhoon Sentinel-2 false-color images and the corresponding relative

517 change in $NDVI_r$ and ΔFVC values are presented in Figure 9. The standard FCC imagery (left

518 panel of Fig. 9) for pre and post-typhoon shows that $NDVI_r$ is more effective in detecting areas

519 of damaged vegetation compared to ΔFVC (right panel, Fig. 9). It was observed that the

520 typhoon-induced damaged vegetation area (i.e., pixels with $NDVI_r$ and ΔFVC of <-50%)

521 detected by NDVIr (106.5 km^2) was greater than that detected by ΔFVC (51.3 km^2). The

522 difference in performance between $NDVI_r$ and ΔFVC in detecting typhoon-induced vegetation

523 damage can be attributed to the fact that the color of the vegetation changed after the typhoon.

524 This change can be detected more accurately by NDVI compared to FVC because the

525 vegetation in the affected areas still existed, and vegetation coverage did not decrease

526 significantly after the event (Wang and Xu, 2018). Thus, NDVI is highly sensitive to the health

527 status of vegetation and a more appropriate approach for assessing the damage to vegetation

528 induced by the typhoon, while FVC is more representative of vegetation coverage status (Wang

529 and Xu, 2018; Jing et al., 2011). Consequently, the dramatic vegetation loss (<-80%) that

530 occurred in mostly wetland vegetation is detected mostly in $NDVIr$. In addition, moderate

531 greenness loss has been identified in natural forests. Furthermore, the decrease of $NDVI_r$ values

532 from higher classes to lower classes indicates that the typhoon has severely damaged the low-

533 lying coastal regions and the wetland vegetation.

534
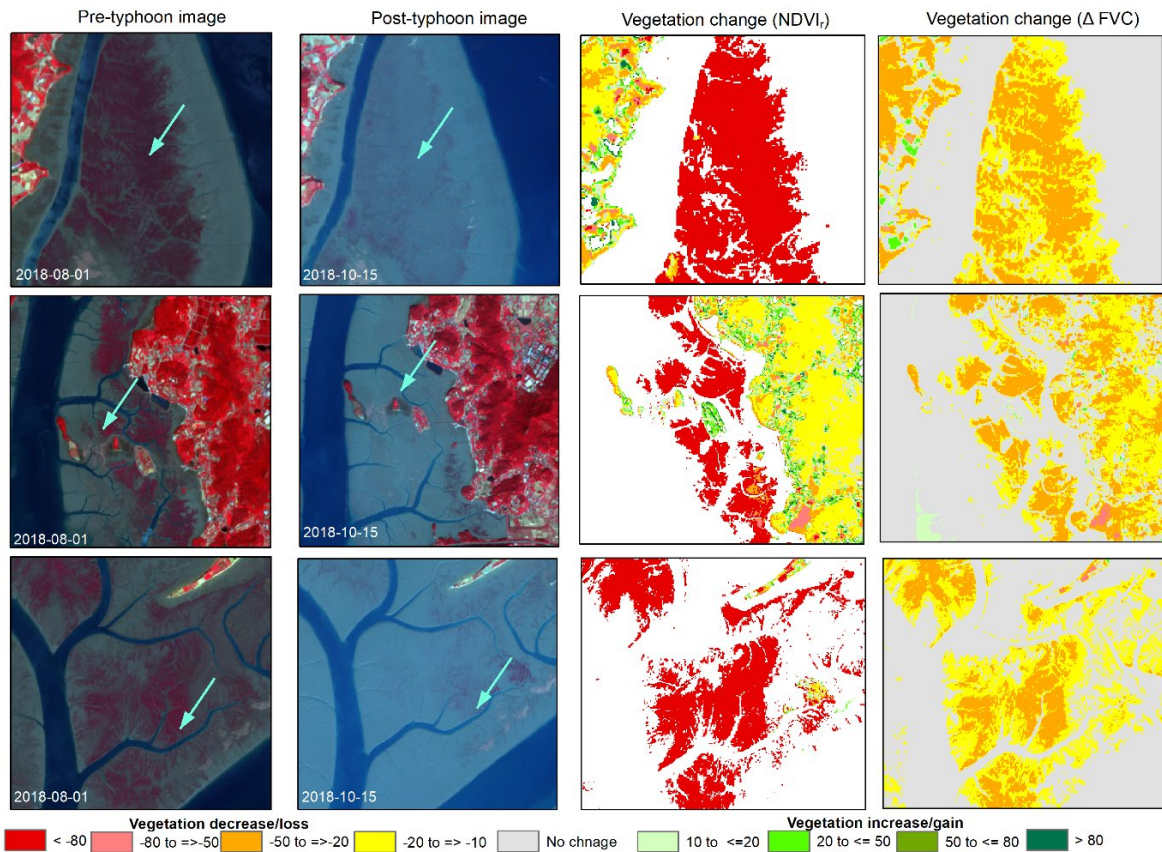
Figure 9. Sentinel-2 MSI standard false color composite images before and after Typhoon Soulik exhibit vegetation damage and the corresponding NDVI$_r$ and ΔFVC (Sentinel-2 MSI level 1C satellite images were downloaded from https://scihub. copernicus.eu/dhus/).

4.1.2 Influence of topography on vegetation damage caused by Typhoon Soulik

The affected area's topography can influence typhoons' impact on vegetation. The interaction between topography and typhoon-generated wind and rain can result in complex and varied patterns of damage across different landscapes (Abbas et al., 2020; Lu et al., 2020; Zhang et al., 2013). This can affect the severity and spatial patterns of vegetation damage. Therefore, the relationship between topography and damaged vegetation has also been established in the present study. For this purpose, high-resolution (5m×5m) DEM data provided by the NGII are used to calculate the region's topographic slope and explore the relationship between topography and typhoon-induced vegetation damage.

It was observed that the elevation varies from 0 to 403 m in the Mopko coastal region, as depicted in Figure 1(b), and the number of trees damaged by Typhoon Soulik showed a decreasing trend at higher elevations (Fig. 10a). The highest number of damaged trees was observed in areas with an elevation of 50m or lower. This is likely due to the fact that these areas are predominantly covered by wetlands, which can be more vulnerable to strong winds

556 associated with typhoons Soulik. In general, low-lying areas may not have the same natural
557 windbreaks and barriers as higher elevations, which can exacerbate the impact of the wind. In
558 addition, low-elevated vegetation may have shallower root systems due to the less stable soil
559 conditions, making them more vulnerable to uprooting during heavy rainfall or strong winds
560 (Zhang et al., 2013; Lugo et al., 1983). A significant difference in the number of decreased
561 ΔNDVI and ΔFVC pixels was observed among different elevation ranges, and a correlation
562 analysis between the number of damaged pixels and elevations showed a negative correlation
563 (i.e., damaged pixels decreased with increasing elevation). The majority of damaged pixels
564 (76.37%) were observed at elevations between 0 and 50m, with a decrease to 13.5% between
565 51 and 100m. Vegetation decreased rapidly at higher elevations, with the percentage of pixels
566 with negative ΔNDVI and ΔFVC decreasing to 6.1% between 100 and 150m and decreasing
567 to 0.02% between 350 and 403m, as depicted in Figure 10(a).

568   On the other hand, Figure 10(b) illustrates the extent of damaged vegetation across
569 different slope ranges. It has been noted that there is a negative correlation between the slope
570 and the percentage of damaged vegetation pixels, indicating that the amount of vegetation
571 damage decreases with a higher slope. For instance, when the slope was between 0-5°,
572 approximately 47.63% of vegetation pixels were damaged. As the slope increased, the
573 percentage of damaged vegetation pixels decreased accordingly, with values of 18.15%,
574 15.01%, 10.71%, 7.74%, 0.73%, and 0.009% observed for slope ranges of 5-10°, 10-15°, 15-
575 20°, 20-30°, 30-40°, and greater than 40°, respectively.

576
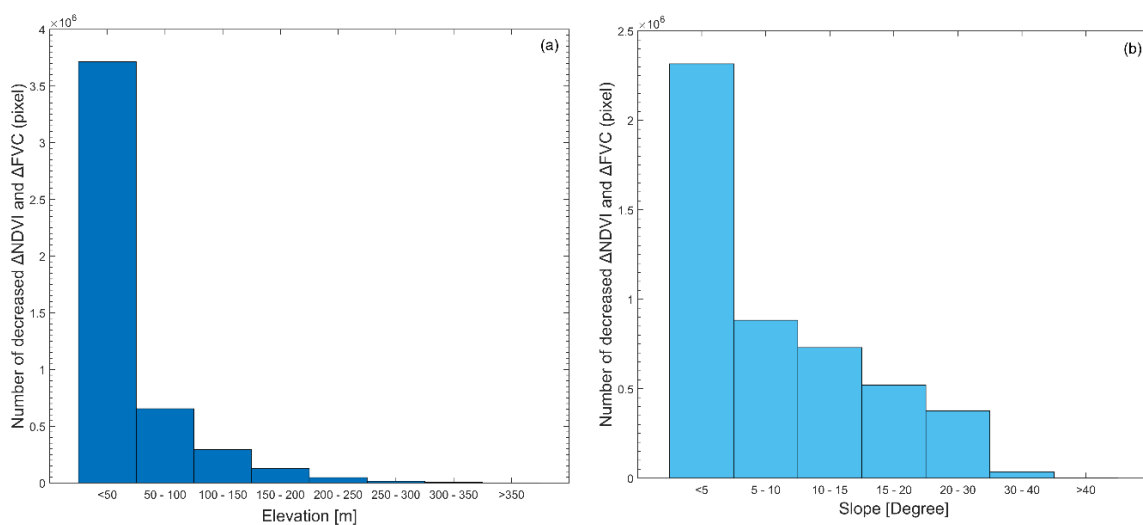
578 Figure 10. The relationship between topography and vegetation damaged due to typhoon
579   Soulik: (a) numbers of damaged vegetation at different elevation ranges, and (b)
580   numbers of damaged vegetation at different slope ranges.

4.2 Coastal morphodynamics over the typhoon period

To understand the coastal morphodynamics over the typhoon period, we classified the entire coastal region into four major coastal landform classes: land, wetland vegetation, wetland, and water (Fig. 11a-b). The accuracy and *kappa* coefficient of the classified maps exhibited a reasonable degree of consistency with the reference data, as illustrated in Table 5. The overall accuracy of the pre-and post-typhoon coastal landform maps was 86.5% and 84.3%, and *kappa* coefficients were 0.82 and 0.79, respectively. The results of the coastal landform classification showed a reduction in wetland vegetation over the typhoon period. Table 6 illustrates that before the typhoon, the area of the wetland vegetation class was 4.21% (77.63 km^2) of the total area of all categories (1845.60 km^2). However, after the hitting of the typhoon storm, the wetland vegetation area reduced to 1.08% (19.90 km^2), recording a degradation of 57.73 km^2 (-74.37%).

Table 5. Accuracy assessment of pre-and post-typhoon classified coastal units.

Coastal Units	Description	Pre-typhoon		Post-typhoon	
		Producer Accuracy (%)	User Accuracy (%)	Producer Accuracy (%)	User Accuracy (%)
Land	Others Land use	90.2	92.0	91.9	90.7
Wetland vegetation	Wetland vegetation	83.4	84.0	85.0	83.3
Wetland	Mudflat/tidal flat	81.4	84.7	77.1	74.0
Water	Waterbody	91.4	85.3	83.2	89.3
Overall accuracy (%)		86.5		84.3	
kappa		0.82		0.79	

The most remarkable gain was the wetland class after the typhoon. This is shown by an increase of wetlands from 258.14 km^2 to 334.97 km^2, i.e., an increase of 29.76% (76.83 km^2) during the analyzed period. Furthermore, the land class has increased by only 0.20% over the typhoon period, i.e., from 45.34% (before the typhoon) to 45.44% (after the typhoon). In addition, it has been noticed the waterbody decreased by 3.09% (20.78 km^2) after the typhoon. Thus, it can be inferred that most wetland vegetation and waterbody have been converted into wetlands, which caused the coastal deterioration.

Table 6. Area changes of different coastal unit during the pre- and post-typhoon periods in the Mokpo coast.

Coastal Units	Area at pre-typhoon	Area at post-typhoon	Changed area

	km^2	%	km^2	%	km^2	%
Land	836.87	45.34	838.55	45.44	1.68	0.20
Wetland Vegetation	77.63	4.21	19.90	1.08	-57.73	-74.37
Wetland	258.14	13.99	334.97	18.15	76.83	29.76
Water	672.95	36.46	652.18	35.34	-20.78	-3.09
Total	1845.60	100.00	1845.60	100.00	---	---

Thereafter, the coastal land transformation model was developed through mutual spatial replacements between coastal units. The land transformation model has identified the nine coastal-change units, as shown in Figure 11(c). The results show that the low land coastal area drastically changed after the typhoon, where the majority of coastal classes have been transformed into wetlands or mudflats. Furthermore, approximately 5.61% of the land area has been replaced by wetlands and water, whereas 83.79% of the wetland area has accreted over the wetland vegetation and water due to the impact of typhoon Soulik (Table 7).
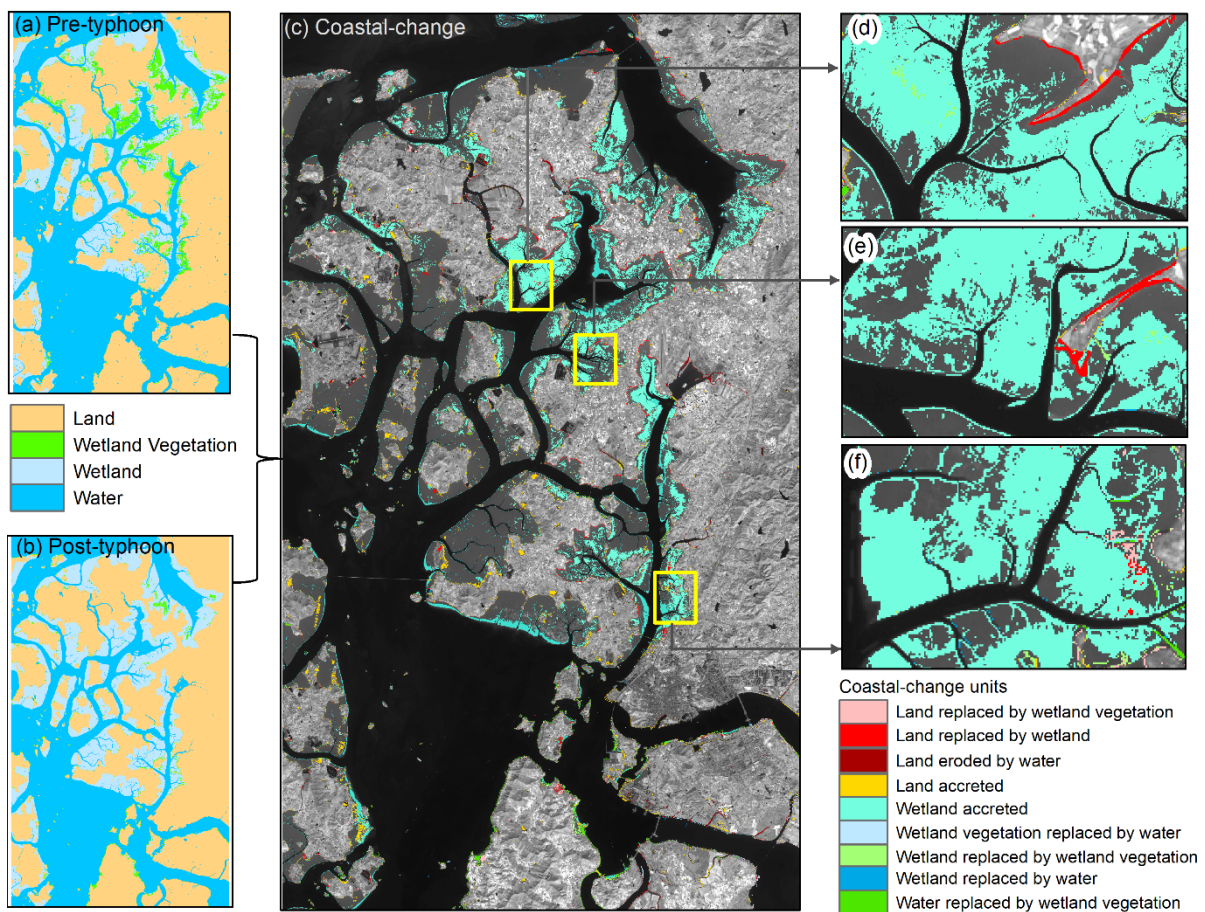
Figure 11. Spatial distribution of coastal-change units along the Mokpo coast due to typhoon Soulik: (a) pre-typhoon classified map, (b) post-typhoon classified map, and (c) coastal land transformation map. Subplots (d, e, and f) show the detailed coastal land

620   transformation.
621
622   Table 7. The details of coastal land transformation classes identify over the typhoon period.

Coastal land transformation	Area (km^2)	%
Land replaced by wetland vegetation	4.59	3.94
Land replaced by wetland	4.41	3.79
Land eroded by water	2.12	1.82
Land accreted	12.88	11.06
Wetland accreted	83.79	71.97
Wetland vegetation replaced by water	2.47	2.12
Wetland replaced by wetland vegetation	1.59	1.36
Wetland replaced by water	1.76	1.52
Water replaced by wetland vegetation	2.82	2.42

623

624 4.3 Sediment resuspension during the pre-and post-typhoon period

625   The spatial distribution of relative suspended sediment concentration has been derived

626 through NDSSI for both before and after typhoon images (Fig. 12). Pre-typhoon SSC patterns

627 have been observed more SSC inside the creeks of the inner-shelf region of the Mokpo coast

628 as compared to the post-typhoon NDSSI image. However, it has been noted that the SSC has

629 significantly increased along the entire coast in the post-typhoon period (Fig. 12b). Therefore,

630 the spatial changes of relative SSC have been determined during the August (pre) and October

631 (post) periods, as depicted in Figure 12(c). In general, a flood always transports many

632 suspended materials and concentrates those materials on the upper surface of the water. After

633 the strong events, the flood-transported suspended material is deposited across the delta. A

634 similar phenomenon was observed in the post-typhoon period due to extensive rainfall, which

635 turned into a coastal flood.

636   On the other hand, it has been observed that the SSC gradually increased as the wind

637 speed increased from the pre to post-typhoon period. The increasing SSC amplitudes indicate

638 the rapid sediment erosion/resuspension over the storm passage. Furthermore, the amplitudes

639 of SSC variations were more visible in shallower water than in deeper water. The effect of

640 typhoons on the SSC variation along the Mokpo coast has been observed through ΔNDSSI

641 distribution (Fig. 12c). The negative ΔNDSSI values represent the increase of SSC due to

642 typhoon-induced strong wind and coastal flooding.
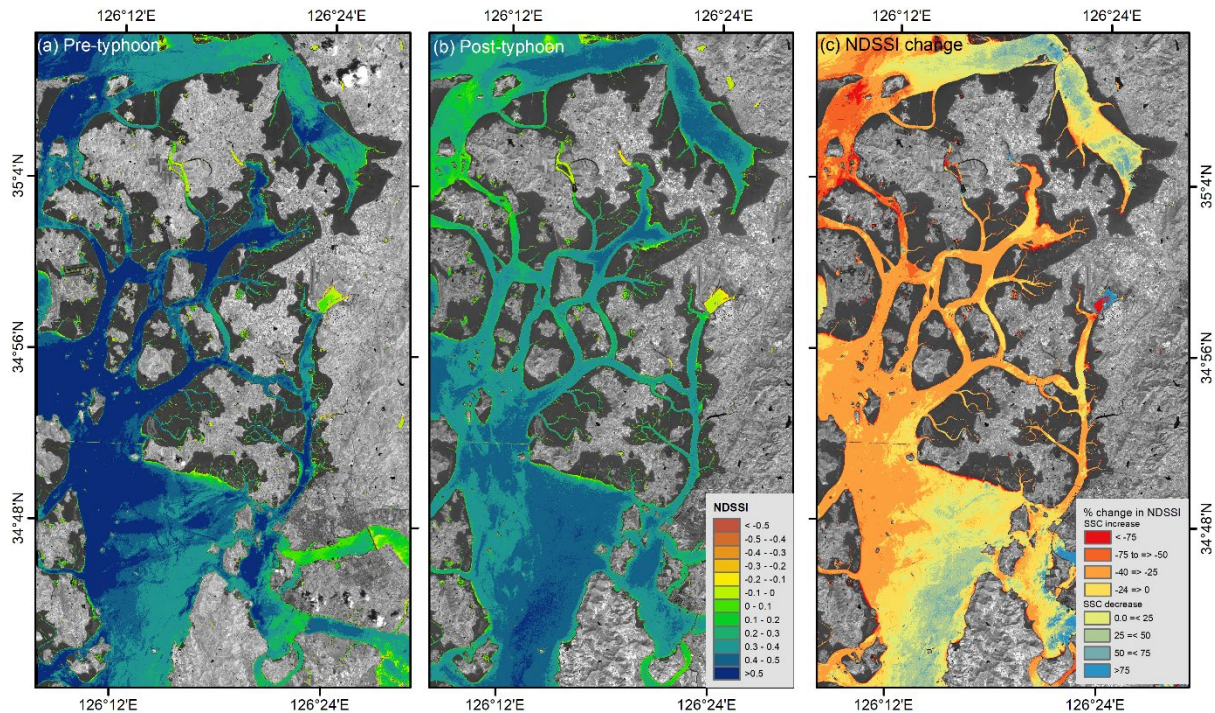
Figure 12. Relative SSC for (a) pre-typhoon and (b) post-typhoon period, while (c) represents the changes in the NDSSI.

Furthermore, a quantitative analysis of SSC has been performed based on the algorithm developed by Choi et al. (2014). During the pre-typhoon period, the SSC in the near shore waters was significantly higher than that of the offshore region (Fig. 13a). The post-typhoon image shows a sharp increase in the SSC distribution, indicating that Typhoon Soulik significantly impacted the SSC variation, with a maximum of >50 g/m^3 (Fig. 13c). In Figures 13(a) and (b), the spring-neap tidal influence broadly regulated the distribution and change of SSC throughout the shallow coastal water. The resuspension of SSC has been observed in the entire study region during the passage of Soulik. The pattern of relative SSC distribution (Fig. 12c) and the empirically derived SSC distribution (Fig. 13c) of pre-and post-typhoon are similar.

The outcomes showed that the storm surge and strong waves have considerably aided the sediment resuspension. Thus, the storm waves played an essential role in increasing bottom stress and stirring the seabed sediment (Gong and Shen, 2009). The transport of sediment during the storm adds another mechanism to the long-term morphological evolution of the Mokpo coast. This research revealed the profound significance of typhoons on inner shelf sedimentation along the coast.
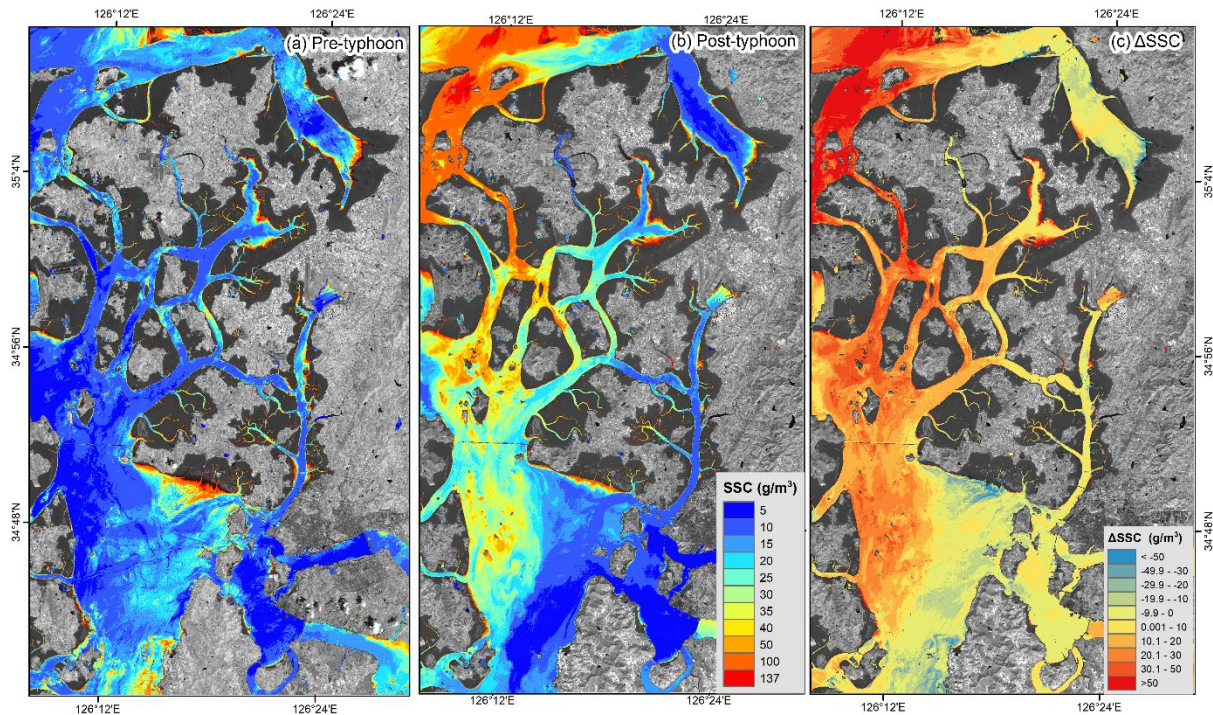
Figure 13. The simulated SSC distribution for the surface water of (a) pre-typhoon, (b) post-typhoon period, and (c) represents the spatial changes of SSC from pre- to post-typhoon.

4.4 Impact on coastal erosion and deposition

The impacts of the severe typhoon storm Soulik at a speed of 62 m/s on the coastline of Mokpo have been determined using the NSM method, considering 38313 transects (10m transect intervals) along the shoreline. Figure 14 shows the shoreline alteration in the entire Mokpo coastal region from the pre- to post-typhoon period, with an accretion of 87.5% transects and erosion of 12.5%. The mean deposition of 28.89m and a mean erosion of -8.29m were recorded (Table 8). The shoreline movement between 0-10m was recorded in the northern part of the coastal region. It has been observed that most transects experienced significant accretion; however, erosion has been observed in a few transects along the southern coastline (Fig. 14). The southern coast experienced sporadic landward movement of the shoreline. In contrast, the rest of the study region experienced significant seaward shoreline movement (Fig. 14 a-e).
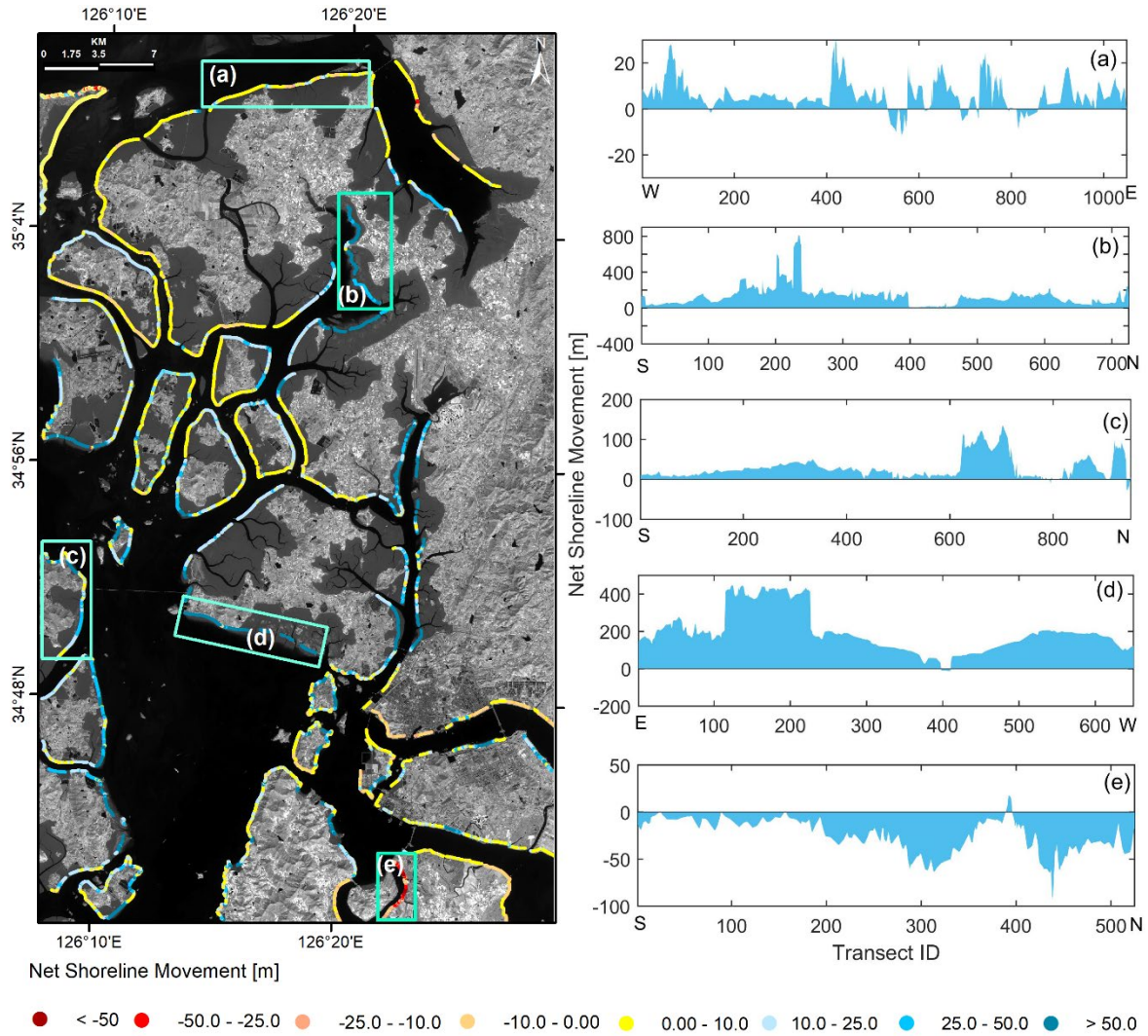
Figure 14. Land water boundary change from the pre-typhoon period to the post-typhoon period based on the NSM method (left panel). Subplots (a-e) show the net movement of the shoreline at different sites.

Table 8. Pre-post typhoon shoreline change statistics based on the NSM model.

NSM statistics	Summary
Total transects	38313
NSM_{mean}	24.24m
$NSM_{mean\ accretion}$	28.89
$NSM_{mean\ erosion}$	-8.29
$NSM_{maximum\ accretion}$	812.54
$NSM_{maximum\ erosion}$	-131.72
Total transect that records accretion	34686
Total transect that records erosion	4955
% of total transect that records accretion	87.5
% of total transect that records erosion	12.5
Overall pre to post-typhoon trend	Accretion

686

687   The wind generated surface water currents that transported and dispersed erogenous
688 material to deep seas areas from pre- to post-typhoon. On the other hand, the coastal flooding
689 induced by the typhoon storm increased the sediment from the land to the near-shore region
690 (Figs. 12c & 13c). This allowed sediment to deposit on the wetland or beach areas. The coastal
691 land transformation map also revealed changes in shoreline shift-area as the wetland accreted
692 class.

693   The net surface area changes along the coastal region have been estimated and are
694 depicted in Figure 15. The total beach area increases and losses throughout the typhoon period
695 were 16.23 km^2 and 1.1 km^2, respectively (Fig. 15f). It was observed that typhoon Soulik has
696 drastically increased the wetland (mudflat). These observations were also supported by other
697 proxies, as discussed above.

698

699
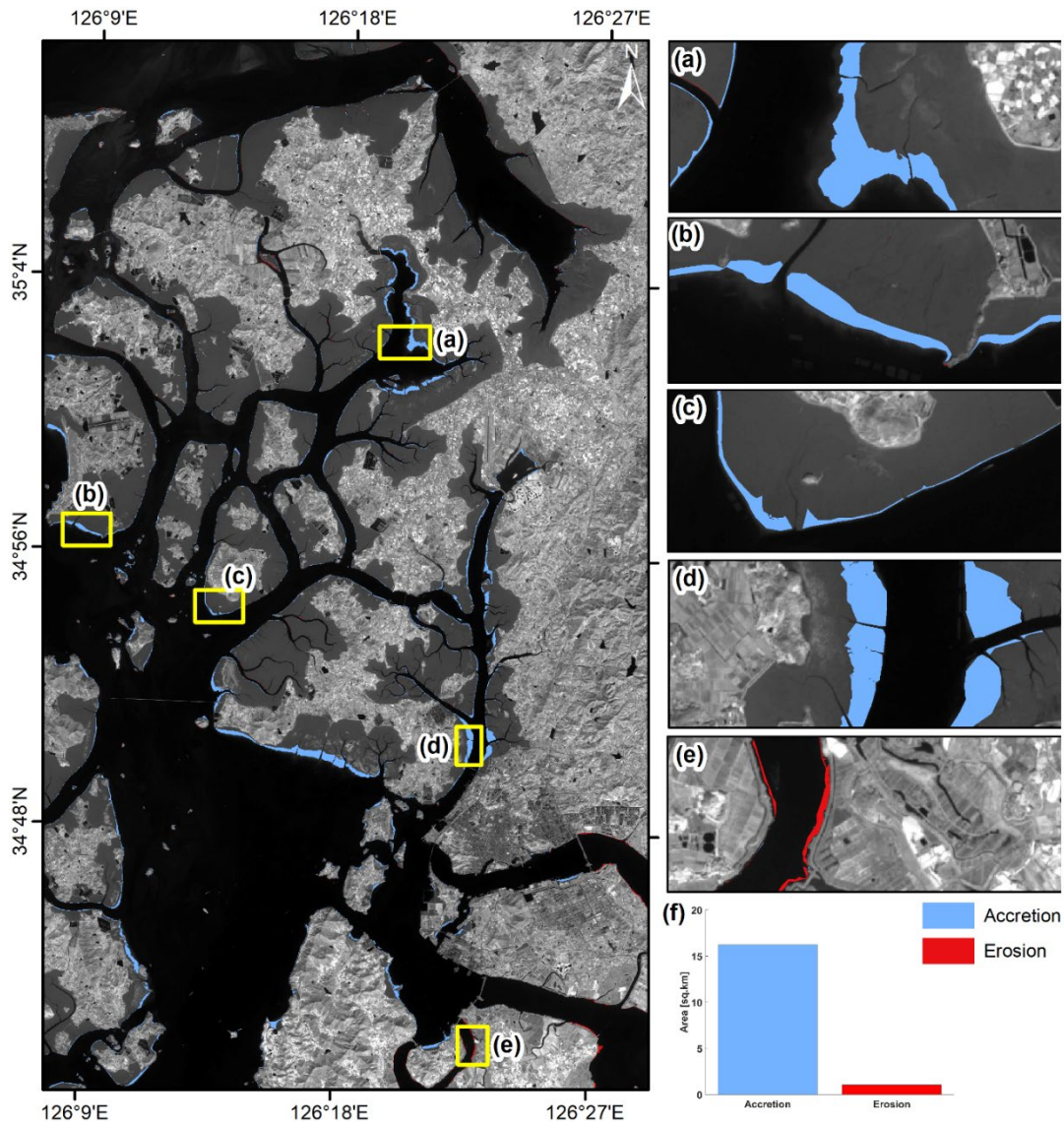
Figure 15. Net surface area changes (i.e., erosion and accretion) due to typhoon Soulik along the Mokpo coast. Subplots (a-d) show extensive accretion, while erosion is shown in plot (e). The bar graph (f) represents the area changes from the pre to post-typhoon period.

4.5 Coastal recovery status after typhoon Soulik

The recovery status of the Mopko coastal region after typhoon Soulik has been analyzed using the NSM and coastal landform change model. For this purpose, another Sentinel-2 MSI level 1C satellite image was downloaded for October 2019 (one year after the typhoon), as listed in Table 1. After that, the coastal landform change model and NSM were performed based on the Sentinel-2 MSI images of October 2018 and 2019 (both images taken during the post-typhoon period) to understand the recovery status of the coastal morphometry. The coastal landform change model exhibits that the wetland vegetation increased drastically after one year of typhoon Soulik, as depicted in Figure 16. Table 9 indicates that approximately 16.52% of the land area has accreted over the wetland and water, whereas 39.71% of the wetland vegetation area has accreted over the wetland and water after the typhoon. Further, the outcome of the coastal recovery status was visually compared with the high-resolution aerial imagery downloaded from the National Land Information Platform web portal (https://map.ngii.go.kr/), indicating good consistency. Thus, the coastal landform change model successfully determined the longer-term recovery status in the topography and landforms of the Mopko coastal area after the typhoon.
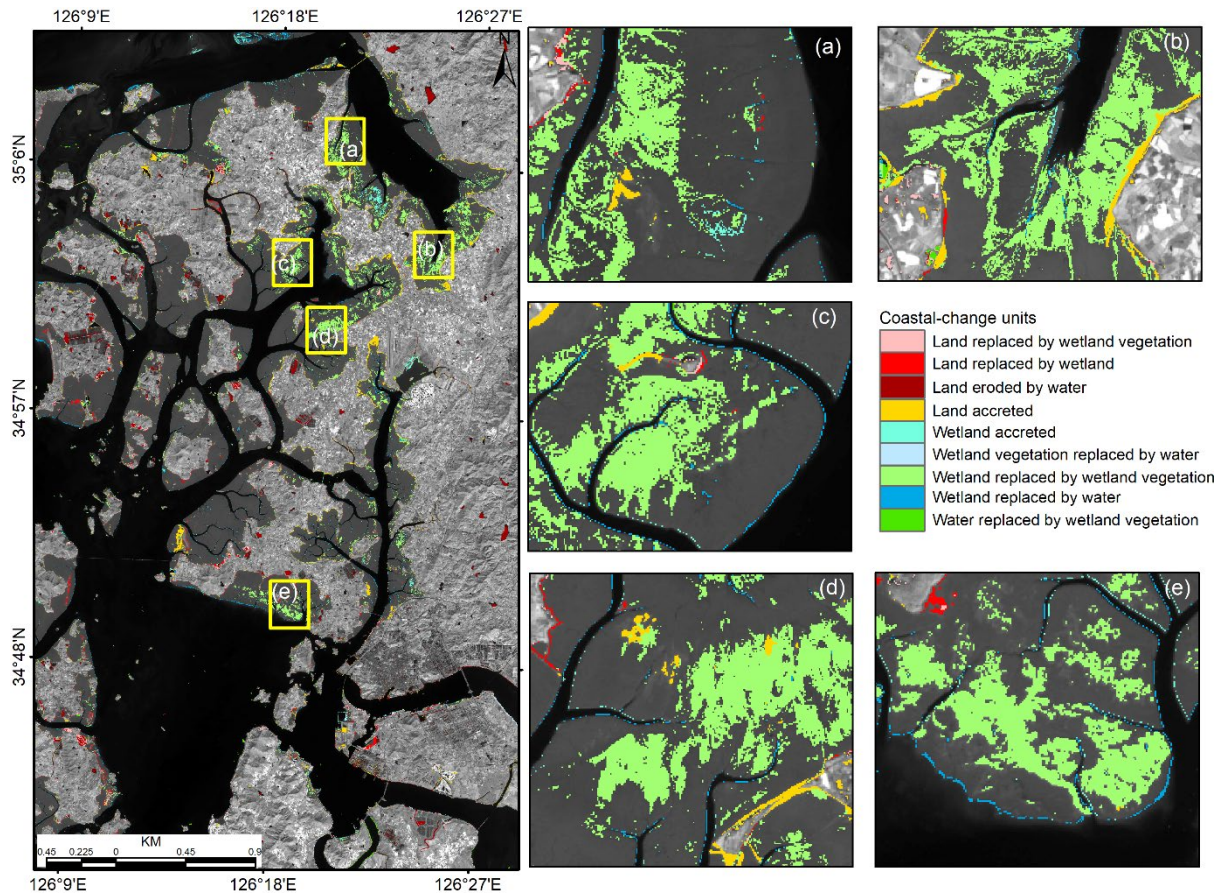
Figure 16. Recovery status of different coastal landforms after typhoon Soulik of Mokpo coastal region, whereas zoom boxes (a-e) show the increase of wetland vegetation at various sites.

Table 9. The details of coastal land transformation classes identify during the post-typhoon period.

Coastal land transformation	Area (km^2)	%
Land replaced by wetland vegetation	4.06	6.67
Land replaced by wetland	4.59	7.54
Land eroded by water	7.23	11.88
Land accreted	10.05	16.52
Wetland accreted	2.82	4.64
Wetland vegetation replaced by water	2.12	3.48
Wetland replaced by wetland vegetation	24.17	39.71
Wetland replaced by water	4.41	7.25
Water replaced by wetland vegetation	1.41	2.32

On the other hand, the short-term effects of a typhoon on the shoreline have also been determined based on the NSM model. The results exhibit the extensive shoreline alteration in the entire Mokpo coastal region after one year of typhoon Soulik, with an accretion of 48.03% transects and erosion of 51.97%. The NSM statistics showed an average shoreline movement

of -1.08m, with a recorded mean erosion of -9.25 and deposition of 7.75m (Table 10). The overall erosion was recorded in response to typhoon Soulik even after one year along the Mopko coastal region. This is due to the extensive damage to wetland vegetation during the typhoon period (Table 7). In addition, it was observed that the wetland experience accretion during the typhoon period, but it made the coastline vulnerable to erosion in the near future. The natural native vegetation and wetland vegetation play a critical role in the shoreline stability of the coastal region due to its anti-erosive nature. This phenomenon was evident in the NSM statistics obtained during the post-typhoon period. Therefore, the use of these models can help predict how the shoreline and adjacent coastal landforms will respond to typhoons, identify vulnerable areas, and inform recovery efforts. This can enhance the area's resilience to natural disasters and reduce the risk of future erosion and other environmental problems.

Table 10. Post-typhoon shoreline change statistics based on the NSM model.

NSM statistics	Summary
Total transects	38313
NSM_{mean}	-1.08m
$NSM_{mean\ accretion}$	7.75
$NSM_{mean\ erosion}$	-9.25
$NSM_{maximum\ accretion}$	44.76
$NSM_{maximum\ erosion}$	-121.14
Total transect that records accretion	18400
Total transect that records erosion	19913
% of total transect that records accretion	51.97
% of total transect that records erosion	48.03
Overall pre to post-typhoon trend	Erosion

5. Conclusion

The objectives of this study were to assess the impact of typhoon Soulik on the coastal ecology, landform, erosion/accretion, suspended sediment movement and associated coastal changes along the Mokpo coast. This research developed an integrated approach for identifying coastal dynamics impacted by typhoons and determining damage severity. The coastline movement, coastal morphodynamics and quantified severity of vegetation damage from the pre- to post-typhoon period have been determined based on the Sentinel-2 MSI images. NDVI and FVC have been used to assess the severity of damage caused by typhoon Soulik on the vegetation. The results showed that about 493.9 km^2 (26.7%) of vegetation had been affected in the Mokpo coastal region. Further, it was observed that 6.1% (112.4 km^2) of vegetated areas in low coastal land were severely damaged. The land transformation model exhibited that the 'wetland'

760 replaced most of the 'wetland-vegetated land' in the post-typhoon period. Also, it has been
761 found that more aggregated vegetation regions were less susceptible to damage.

762   The SSC of the Mokpo coastal region is higher in the post-typhoon period compared to
763 pre-typhoon time. The SSC variation influenced the coastal accretion and changed the deltaic
764 islands. The NDSSI and empirical-based SSC distribution of pre- and post-typhoon images
765 exhibit sedimentation drastically increased after the typhoon. The land accretion process also
766 dominated during the pre- to post-typhoon period. The wetlands and water have replaced
767 approximately 9.77% of the land area. On the other hand, 65.52% of the wetland area has
768 accreted over the wetland vegetation and water. Shoreline change analysis is also performed to
769 understand erosion and accretion in coastal regions. Typhoon Soulik accelerated shoreline
770 movement, affecting the local environmental condition, biodiversity imbalance, and aerial
771 change. In addition, 87.35% of shoreline transects experienced seaward migration over the
772 typhoon period. The wetland experience accretion in a shorter period, but it made the coastline
773 vulnerable to erosion in the near future because the natural native vegetation and wetland
774 vegetation are crucial factors in shoreline stability of the coastal region due to its anti-erosive
775 nature. This phenomenon was evident in the NSM and coastal landforms change model
776 obtained during the post-typhoon period. It can be concluded that the Mokpo coastal ecosystem
777 has been devastated by this extreme event. Although the observed changes are not alarming,
778 shoreline protection measures still need to be addressed, especially the reforestation in wetland
779 or mudflat regions. The outputs of the present study are needed to better understand the
780 sediment transport process and estuary changes during the pre-and post-typhoon period. It can
781 also be used to develop appropriate strategies to protect natural ecosystems and post-disaster
782 rehabilitation.
783

784 **Acknowledgments**
785 This paper was supported by research funds for newly appointed professors of Gangneung-
786 Wonju National University in 2021. The authors are thankful to the European Space Agency
787 (ESA) for providing free satellite images. The authors would like to thank the esteemed
788 reviewers for their valuable comments and suggestions that helped improve the manuscript.
789

790 **Funding**
791 This work was supported by the National Research Foundation of Korea (NRF) grant funded
792 by the Korea government (NRF-2021R1C1C2003316) and Basic Science Research Program

793 through the National Research Foundation of Korea (NRF) funded by the Ministry of
794 Education (2021R1A6A1A03044326).

795

796 **References**

797 Abbas, S., Nichol, J. E., Fischer, G. A., Wong, M. S., and Irteza, S. M.: Impact assessment of
798   a super-typhoon on Hong Kong's secondary vegetation and recommendations for
799   restoration of resilience in the forest succession, Agricultural and Forest Meteorology,
800   280, 107784, https://doi.org/10.1016/j.agrformet.2019.107784, 2020.

801 Adhikari, M. D., Maiti, S., Bera, A., and Chaudhury, N. R.: Post-tsunami adjustment of coral
802   reef platform and other morphometric changes in Landfall Island, North Andaman—
803   An integrated field and remote sensing-based approach, Regional Studies in Marine
804   Science, 48, 101975, https://doi.org/10.1016/j.rsma.2021.101975, 2021.

805 Altman, J., Doležal, J., Černý, T., and Song, J. S.: Forest response to increasing typhoon
806   activity on the Korean peninsula: evidence from oak tree-rings, Global Change Biology,
807   19(2), 498-504, https://doi.org/10.1111/gcb.12067, 2013.

808 Amiri, R., Weng, Q., Alimohammadi, A., and Alavipanah, S. K.: Spatial–temporal dynamics
809   of land surface temperature in relation to fractional vegetation cover and land use/cover
810   in the Tabriz urban area, Iran, Remote sensing of environment, 113(12), 2606-2617,
811   https://doi.org/10.1016/j.rse.2009.07.021, 2009.

812 Arisanty, D., and Saputra, A. N.: Remote sensing studies of suspended sediment concentration
813   variation in Barito Delta, In IOP Conference Series: Earth and Environmental Science,
814   98(1), 012058, 2017.

815 Aswatha, S. M., Mukherjee, J., Biswas, P. K., and Aikat, S.: Unsupervised classification of
816   land cover using multi-modal data from multispectral and hybrid-polarimetric SAR
817   imageries, International Journal of Remote Sensing, 41(14), 5277-5304,
818   https://doi.org/10.1080/01431161.2020.1731771, 2020.

819 Awad, M., and El-Sayed, H. M.: The analysis of shoreline change dynamics and future
820   predictions using automated spatial techniques: Case of El-Omayed on the
821   Mediterranean coast of Egypt, Ocean & Coastal Management, 205, 105568,
822   https://doi.org/10.1016/j.ocecoaman.2021.105568, 2021.

823 Bao, A., Huang, Y., Ma, Y., Guo, H., and Wang, Y.: Assessing the effect of EWDP on
824   vegetation restoration by remote sensing in the lower reaches of Tarim River,
825   Ecological Indicators, 74, 261-275, https://doi.org/10.1016/j.ecolind.2016.11.007,

826   2017.

827   Bhowmik, A. K., and Cabral, P.: Cyclone Sidr impacts on the Sundarbans floristic diversity,
828   Earth Science Research, 2(2), 62, http://dx.doi.org/10.5539/esr.v2n2p62, 2013.

829   Bhuiyan, Md. J. A. N. and Dutta, D.: Analysis of flood vulnerability and assessment of the
830   impacts in coastal zones of Bangladesh due to potential sea-level rise, Natural Hazards,
831   61(2), 729-743, https://doi.org/10.1007/s11069-011-0059-3, 2012.

832   Bian, S., Hu, Z., Liu, J., and Zhu, Z.: Sediment suspension and the dynamic mechanism during
833   storms in the Yellow River Delta, Environmental Monitoring and Assessment, 189(1),
834   1-13, https://doi.org/10.1007/s10661-016-5688-2, 2017.

835   Bishop-Taylor, R., Nanson, R., Sagar, S., and Lymburner, L.: Mapping Australia's dynamic
836   coastline at mean sea level using three decades of Landsat imagery, Remote Sensing of
837   Environment, 267, 112734, https://doi.org/10.1016/j.rse.2021.112734, 2021.

838   Byun, D. S., Wang, X. H., and Holloway, P. E.: Tidal characteristic adjustment due to dyke
839   and seawall construction in the Mokpo Coastal Zone, Korea, Estuarine, Coastal and
840   Shelf Science, 59(2), 185-196, https://doi.org/10.1016/j.ecss.2003.08.007, 2004.

841   Cakir, H. I., Khorram, S., and Nelson, S. A.: Correspondence analysis for detecting land cover
842   change, Remote Sensing of Environment, 102 (3-4), 306-317, https://doi.org/
843   10.1016/j.rse.2006.02.023, 2006.

844   Carlson, T. N., and Ripley, D. A.: On the relation between NDVI, fractional vegetation cover,
845   and leaf area index, Remote sensing of Environment, 62(3), 241-252,
846   https://doi.org/10.1016/S0034-4257(97)00104-1, 1997.

847   Cha, E. J., Yun, S. G., Moon, I. J., and Kim, D. H.: Binary interaction of typhoons Soulik and
848   Cimaron in 2018–Part I: Observational characteristics and forecast error, Tropical
849   Cyclone Research and Review, 10(1), 32-42, https://doi.org/10.1016/j.tcrr.
850   2021.03.001, 2021.

851   Charrua, A. B., Padmanaban, R., Cabral, P., Bandeira, S., and Romeiras, M. M.: Impacts of the
852   tropical cyclone idai in mozambique: A multi-temporal Landsat satellite imagery
853   analysis, Remote Sensing, 13(2), 201, https://doi.org/10.3390/rs13020201, 2021.

854   Chau, P. M., Wang, C. K., and Huang, A. T.: The spatial-temporal distribution of GOCI-
855   derived suspended sediment in Taiwan coastal water induced by typhoon Soudelor,
856   Remote Sensing, 13(2), 194, https://doi.org/10.3390/rs13020194, 2021.

857   Choi, M. K., Choi, H. G., Moon, H. B., Yu, J., Kang, S. K., and Choi, S. K.: Sources and
858   distributions of organic wastewater compounds on the Mokpo Coast of Korea, Fisheries

and Aquatic Sciences, 10(4), 205-214, https://doi.org/10.5657/fas.2007.10.4.205, 2007.

Choi, J. K., Park, Y. J., Ahn, J. H., Lim, H. S., Eom, J., and Ryu, J. H.: GOCI, the world's first geostationary ocean color observation satellite, for the monitoring of temporal variability in coastal water turbidity, Journal of Geophysical Research: Oceans, 117(C9), https://doi.org/10.1029/2012JC008046, 2012.

Choi, J. K., Park, Y. J., Lee, B. R., Eom, J., Moon, J. E., and Ryu, J. H.: Application of the Geostationary Ocean Color Imager (GOCI) to mapping the temporal dynamics of coastal water turbidity, Remote Sensing of Environment, 146, 24-35, https://doi.org/10.1016/j.rse.2013.05.032, 2014.

Choi, K.: Morphology, sedimentology and stratigraphy of Korean tidal flats–Implications for future coastal managements, Ocean & Coastal Management, 102, 437-448, https://doi.org/10.1016/j.ocecoaman.2014.07.009, 2014.

Chu, T., Guo, X.,and Takeda, K.: Remote sensing approach to detect post-fire vegetation regrowth in Siberian boreal larch forest, Ecological Indicators, 62, 32-46, https://doi.org/10.1016/j.ecolind.2015.11.026, 2016.

Congalton, R. G.: A review of assessing the accuracy of classifications of remotely sensed data, Remote Sensing of Environment, 37(1), 35-46, https://doi.org/10.1016/0034-4257(91)90048-B, 1991.

Dai, C, Howat, I. M., Larour, E., and Husby, E.: Coastline extraction from repeat high resolution satellite imagery, Remote Sensing of Environment, 229, 260–270, https://doi.org/10.1016/j.rse.2019.04.010, 2019.

Dail, M. B., Corbett, D. R., and Walsh, J. P.: Assessing the importance of tropical cyclones on continental margin sedimentation in the Mississippi delta region, Continental Shelf Research, 27(14), 1857-1874, https://doi.org/10.1016/j.csr.2007.03.004, 2007.

Datta, D. and Deb, S.: Analysis of coastal land use/land cover changes in the Indian Sunderbans using remotely sensed data, Geospatial Information Science, 15(4), 241-250, https://doi.org/10.1080/10095020.2012.714104, 2012.

Deabes, E. A.: Applying ArcGIS to Estimate the Rates of Shoreline and Back-Shore Area Changes along the Nile Delta Coast, Egypt, International Journal of Geosciences, 8(03), 332, DOI: 10.4236/ijg.2017.83017, 2017.

Eastman, J. R., Sangermano, F., Machado, E. A., Rogan, J., and Anyamba, A.: Global trends in seasonality of normalized difference vegetation index (NDVI), 1982–2011, Remote Sensing, 5(10), 4799-4818, https://doi.org/10.3390/rs5104799, 2013.

892 Eom, J., Lee, C., Jang, J., Choi, J. K., and Park, S.: Study on environmental change monitoring
893   between shoreline change and suspended sediment concentration using Landsat images
894   in Nakdong river, Korea, In IEEE International Geoscience and Remote Sensing
895   Symposium (IGARSS), 3607-3609, 2017.

896 ERDAS.: ERDAS Imagine Tour Guides (Atlanta, GA: ERDAS Inc.), 1997.

897 ESA.: Multispectral instrument (MSI) overview, Retrieved 07th September, 2022, from
898   https://sentinels.copernicus.eu/web/sentinel/technical-guides/sentinel-2-msi, 2020.

899 Filgueiras, R., Mantovani, E. C., Althoff, D., Fernandes Filho, E. I., and Cunha, F. F. D.: Crop
900   NDVI monitoring based on sentinel 1, Remote Sensing, 11(12), 1441, https://doi.org
901   /10.3390/rs11121441, 2019.

902 Ge, J., Meng, B., Liang, T., Feng, Q., Gao, J., Yang, S., ... and Xie, H.: Modeling alpine
903   grassland cover based on MODIS data and support vector machine regression in the
904   headwater region of the Huanghe River, China, Remote Sensing of Environment, 218,
905   162-173, https://doi.org/10.1016/j.rse.2018.09.019, 2018.

906 Goff, J. A., Allison, M. A., and Gulick, S. P.: Offshore transport of sediment during cyclonic
907   storms: Hurricane Ike (2008), Texas Gulf Coast, USA, Geology, 38(4), 351-354,
908   https://doi.org/10.1130/G30632.1, 2010.

909 Gong, W. and Shen, J.: Response of sediment dynamics in the York River Estuary, USA to
910   tropical cyclone Isabel of 2003, Estuarine, Coastal and Shelf Science, 84(1), 61-74,
911   https://doi.org/10.1016/j.ecss.2009.06.004, 2009.

912 Halder, B. and Bandyopadhyay, J.: Monitoring the tropical cyclone 'Yass' and
913   'Amphan'affected flood inundation using Sentinel-1/2 data and Google Earth Engine,
914   Modeling Earth Systems and Environment, 1-16, https://doi.org/10.1007/s40808-022-
915   01359-w, 2022.

916 Hopper, M.: WXTide32 Version 4.0. Free Software Foundation Inc., Cambridge, 2004.

917 Hoque, M. A. A., Phinn, S., Roelfsema, C., and Childs, I.: Assessing tropical cyclone impacts
918   using object-based moderate spatial resolution image analysis: a case study in
919   Bangladesh, International Journal of Remote Sensing, 37(22), 5320-5343,
920   https://doi.org/10.1080/01431161.2016.1239286, 2016.

921 Hossain, A. K. M. A., Jia, Y., and Chao, X.: Development of remote sensing based index for
922   estimating/mapping suspended sediment concentration in river and lake environments,
923   In Proceedings of 8th international symposium on ECOHYDRAULICS, 435, 578-585,
924   2010.

925 Hossain, A. A., Mathias, C., and Blanton, R.: Remote sensing of turbidity in the Tennessee
926   River using Landsat 8 satellite, Remote Sensing, 13(18), 3785, https://doi.org/
927   10.3390/rs13183785, 2021.

928 Hu, T. and Smith, R. B.: The impact of Hurricane Maria on the vegetation of Dominica and
929   Puerto Rico using multispectral remote sensing, Remote Sensing, 10(6), 827,
930   https://doi.org/10.3390/rs10060827, 2018.

931 Hwang, D. J., Choi, J. K., Eom, J., Ryu, J. H., and Woo, H. J.: Long-term monitoring of
932   suspended sediments concentration using GOCI and field data in Han-river estuary,
933   Korea, In 2016 IEEE International Geoscience and Remote Sensing Symposium, 2465-
934   2467, 2016.

935 Hwang, S., Son, S., Lee, C., and Yoon, H. D.: Quantitative assessment of inundation risks from
936   physical contributors associated with future storm surges: a case study of Typhoon
937   Maemi (2003), Natural Hazards, 104(2), 1389-1411, https://doi.org/10.1007/s11069-
938   020-04225-z, 2020.

939 Jing, X., Yao, W. Q., Wang, J. H., and Song, X. Y.: A study on the relationship between
940   dynamic change of vegetation coverage and precipitation in Beijing's mountainous
941   areas during the last 20 years, Mathematical and Computer Modelling, 54(3-4), 1079-
942   1085, https://doi.org/10.1016/j.mcm.2010.11.038, 2011.

943 Kang, J. W.: Changes in tidal characteristics as a result of the construction of sea-dike/sea-
944   walls in the Mokpo coastal zone in Korea, Estuarine, Coastal and Shelf Science, 48 (4),
945   429-438, https://doi.org/10.1006/ecss.1998.0464, 1999.

946 Kang, J. W. and Jun, K. S.: Flood and ebb dominance in estuaries in Korea, Estuarine, Coastal
947   and Shelf Science, 56 (1), 187-196, https://doi.org/10.1016/S0272-7714(02)00156-7,
948   2003.

949 Kang, J. W., Moon, S. R., Lee, D. S., and Lee, J. L.: Surge-Wave Combined Inundation at
950   Mokpo North Harbour, Korea, Journal of Coastal Research, 1081-1085, 2007.

951 Kang, K., Jo, H. J., and Kim, Y.: Ocean responses to Typhoon Soulik (1819) around Korea,
952   Ocean Science Journal, 55(3), 445-457, https://doi.org/10.1007/s12601-020-0030-x,
953   2020.

954 Kang, K. and Moon, I. J.: Sea Surface Height Changes due to the Tropical Cyclone-Induced
955   Water Mixing in the Yellow Sea, Korea, Frontiers of Earth Science, 10, 826582, doi:
956   10.3389/feart.2022.826582, 2022.

957 Kavan, J., Wieczorek, I., Tallentire, G. D., Demidionov, M., Uher, J., and Strzelecki, M. C.:

958   Estimating Suspended Sediment Fluxes from the Largest Glacial Lake in Svalbard to

959   Fjord System Using Sentinel-2 Data: Trebrevatnet Case Study, Water, 14(12), 1840,

960   https://doi.org/10.3390/w14121840, 2022.

961 Kermani, S., Boutiba, M., Guendouz, M., Guettouche, M. S., and Khelfani, D.: Detection and

962   analysis of shoreline changes using geospatial tools and automatic computation: Case

963   of jijelian sandy coast (East Algeria), Ocean & Coastal Management, 132, 46-58,

964   https://doi.org/10.1016/j.ocecoaman.2016.08.010, 2016.

965 Keukelaere, L. De, Sterckx, S., Adriaensen, S., Knaeps, E., Reusen, I., Giardino, C., ... and

966   Vaiciute, D.: Atmospheric correction of Landsat-8/OLI and Sentinel-2/MSI data using

967   iCOR algorithm: validation for coastal and inland waters, European Journal of Remote

968   Sensing, 51(1), 525-542, https://doi.org/10.1080/22797254.2018.1457937, 2018.

969 Kim, Y. C.: Handbook of coastal and ocean engineering, World Scientific, 2010.

970 Kim, J. M., Bae, J., Son, S., Son, K., and Yum, S. G.: Development of model to predict natural

971   disaster-induced financial losses for construction projects using deep learning

972   techniques. Sustainability, 13(9), 5304, https://doi.org/10.3390/su13095304, 2021.

973 KMA.: Typhoon White Book, Available at https://www.kma.go.kr/download_01

974   /typhoon/typwhitebook_2011.pdf, 2011.

975 KMA.: 2018 annual report, available at https://www.kma.go.kr/download_01/Annual

976   _Report_2018.pdf , 2018.

977 Konda, V. G. R. K., Chejarla, V. R., Mandla, V. R., Voleti, V., and Chokkavarapu, N.:

978   Vegetation damage assessment due to Hudhud cyclone based on NDVI using Landsat-

979   8 satellite imagery, Arabian Journal of Geosciences, 11(2), 1-11,

980   https://doi.org/10.1007/s12517-017-3371-8, 2018.

981 Kumar, R., Rani, S., and Maharana, P.: Assessing the impacts of Amphan cyclone over West

982   Bengal, India: a multi-sensor approach, Environmental Monitoring and Assessment,

983   193(5), 1-21, https://doi.org/10.1007/s10661-021-09071-5, 2021.

984 Kwon, J. I., Choi, J. W., Lee, J. C., Min, I. K., and Park, K. S.: Spatio-temporal Characteristics

985   of Storm Surge Events in the Korean Peninsula, Journal of Coastal Research, 85

986   (10085), 891-895, 2018.

987 Landis, J. R. and Koch, G. G.: An application of hierarchical kappa-type statistics in the

988   assessment of majority agreement among multiple observers, Biometrics, 363-374,

989   1977.

990 Lee, J. K., Kim, J. O., and Oh, Y. S.: Development of Coastal Safety Mapping System by

Vulnerability Assessment of Tidal Creeks, Journal of Coastal Research, 114, 459-463, 2021.

Lee, M. S., Park, K., Chung, J. Y., Ahn, Y. H., and Moon, J. E.: Estimation of coastal suspended sediment concentration using satellite data and oceanic in-situ measurements, Korean Journal of Remote Sensing, 27(6), 677-692, 2011.

Lee, S. W., Nam, S. H., and Kim, D. J.: Estimation of marine winds in and around typhoons using multi-platform satellite observations: Application to Typhoon Soulik (2018), Frontiers of Earth Science, 16(1), 175-189, https://doi.org/10.1007/s11707-020-0849-6, 2022.

Lee, Y.: 2014. Coastal planning strategies for adaptation to sea level rise: A case study of Mokpo, Korea, Journal of Building Construction and Planning Research, 2(1), DOI:10.4236/jbcpr.2014.21007, 2014.

Lee, Y. K., Choi, J. K., and Lee, H. J.: A study on seasonal dynamics of suspended particulate matter in Korean coastal waters using GOCI, Journal of Coastal Research, 102 (SI), 232-245, https://doi.org/10.2112/SI102-029.1, 2020.

Li, K. and Li, G. S.: Risk assessment on storm surges in the coastal area of Guangdong Province, Natural Hazards, 68(2), 1129-1139, https://doi.org/10.1007/s11069-013-0682-2, 2013.

Li, Y., Li, H., Qiao, L., Xu, Y., Yin, X., and He, J.: Storm deposition layer on the Fujian coast generated by Typhoon Saola (2012), Scientific reports, 5(1), 1-7, https://doi.org/10.1038/srep14904, 2015.

Li, Y. and Li, X.: Remote sensing observations and numerical studies of a super typhoon-induced suspended sediment concentration variation in the East China Sea, Ocean Modelling, 104, 187-202, https://doi.org/10.1016/j.ocemod.2016.06.010, 2016.

Liu, Y., Wu, L., and Yue, H.: Biparabolic NDVI-Ts space and soil moisture remote sensing in an arid and semi-arid area, Canadian Journal of Remote Sensing, 41(3), 159-169, https://doi.org/10.1080/07038992.2015.1065705, 2015.

Lu, J., Jiang, J., Li, A., and Ma, X.: Impact of Typhoon Chan-hom on the marine environment and sediment dynamics on the inner shelf of the East China Sea: In-situ seafloor observations, Marine Geology, 406, 72-83, https://doi.org/10.1016/j.margeo.2018.09.009, 2018.

Lu, L., Wu, C., and Di, L.: Exploring the spatial characteristics of typhoon-induced vegetation damages in the southeast coastal area of China from 2000 to 2018, Remote Sensing,

1024   12(10), 1692, https://doi.org/10.3390/rs12101692, 2020.

1025 Lugo, A. E., Applefield, M., Pool, D. J., and McDonald, R. B.: The impact of Hurricane David

1026   on the forests of Dominica, Canadian Journal of Forest Research, 13(2), 201-211,

1027   https://doi.org/10.1139/x83-029, 1983.

1028 Maiti, S., and Bhattacharya, A. K.: Shoreline change analysis and its application to prediction:

1029   A remote sensing and statistics based approach, Marine Geology 257(1-4), 11-23,

1030   https://doi.org/10.1016/j.margeo.2008.10.006, 2009.

1031 Maiti, S. and Bhattacharya, A. K.: A three-unit-based approach in coastal-change studies using

1032   Landsat images, International Journal of Remote Sensing, 32(1), 209-229,

1033   https://doi.org/10.1080/01431160903439965, 2011.

1034 Mallick, B., Ahmed, B., and Vogt, J.: Living with the risks of cyclone disasters in the

1035   southwestern coastal region of Bangladesh, Environments, 4(1), 13,

1036   https://doi.org/10.3390/environments4010013, 2017.

1037 McFeeters, S. K.: The use of the Normalized Difference Water Index (NDWI) in the

1038   delineation of open water features, International Journal of Remote Sensing, 17(7),

1039   1425–1432, https://doi.org/10.1080/01431169608948714, 1996.

1040 Member Report: Member Report, Republic of Korea. ESCAP/WMO Typhoon Committee, 13th

1041   Integrated Workshop, Chiang Mai, Thailand, 5-9 November 2018 (Avialable at

1042   https://www.typhooncommittee.org/13IWS/Members13IWS.html, lat access 28th

1043   April, 2023), 2018.

1044 Min, J. E., Ryu, J. H., Ahn, Y. H., and Lee, K. S.: Monitoring suspended sediment distribution

1045   using Landsat TM/ETM+ data in coastal waters of Seamangeum, Korea, In Proceedings

1046   of the KSRS Conference, The Korean Society of Remote Sensing, 340-343, 2004.

1047 Min, J. E., Ahn, Y. H., Lee, K. S., and Ryu, J. H.: Development of Suspended Sediment

1048   Algorithm for Landsat TM/ETM+ in Coastal Sea Waters-A Case Study in Saemangeum

1049   Area, Korean Journal of Remote Sensing, 22(2), 87-99, 2006.

1050 Min, J. E., Ryu, J. H., Lee, S., and Son, S.: Monitoring of suspended sediment variation using

1051   Landsat and MODIS in the Saemangeum coastal area of Korea, Marine Pollution

1052   Bulletin, 64(2), 382-390, https://doi.org/10.1016/j.marpolbul.2011.10.025, 2012.

1053 Min, J. E., Choi, J. K., Yang, H., Lee, S., and Ryu, J. H.: Monitoring changes in suspended

1054   sediment concentration on the southwestern coast of Korea, Journal of Coastal

1055   Research, 70, 133-138, 2014.

1056 Mishra, M., Acharyya, T., Santos, C. A. G., da Silva, R. M., Kar, D., Kamal, A. H. M., and

Raulo, S.: Geo-ecological impact assessment of severe cyclonic storm Amphan on Sundarban mangrove forest using geospatial technology, Estuarine, Coastal and Shelf Science, 260, 107486, https://doi.org/10.1016/j.ecss.2021.107486, 2021a.

Mishra, M., Santos, C. A. G., da Silva, R. M., Rana, N. K., Kar, D., and Parida, N. R.: Monitoring vegetation loss and shoreline change due to tropical cyclone Fani using Landsat imageries in Balukhand-Konark Wildlife Sanctuary, India, Journal of Coastal Conservation, 25(6), 1-11, https://doi.org/10.1007/s11852-021-00840-5, 2021b.

Moon, I. J., Oh, I. S., Murty, T., and Youn, Y. H.: Causes of the unusual coastal flooding generated by Typhoon Winnie on the west coast of Korea, Natural Hazards, 29(3), 485-500, https://doi.org/10.1023/A:1024798718572, 2003.

Na, C. K.: Heavy metals in sediments and organisms from tidal flats along the Mokpo coastal area, Economic and Environmental Geology, 37(3), 335-345, 2004.

Nandi, G., Neogy, S., Roy, A. K., and Datta, D.: Immediate disturbances induced by tropical cyclone Fani on the coastal forest landscape of eastern India: A geospatial analysis, Remote Sensing Applications: Society and Environment, 20, 100407, https://doi.org/10.1016/j.rsase.2020.100407, 2020.

Nayak, S.: Use of satellite data in coastal mapping, Indian Cartographer, 22(147-157), 1, 2002.

NGII.: Digital elevation model, NGII (National Geographical Information Institute), the Ministry of Land, Infrastructure and Transport, Korea, 2018.

Parida, B. R., Behera, S. N., Oinam, B., Patel, N. R., and Sahoo, R. N.: Investigating the effects of episodic Super-cyclone 1999 and Phailin 2013 on hydro-meteorological parameters and agriculture: An application of remote sensing, Remote Sensing Applications: Society and Environment, 10, 128-137, https://doi.org/10.1016/j.rsase.2018.03.010, 2018.

Park, J. H., Yeo, D. E., Lee, K., Lee, H., Lee, S. W., Noh, S., ..., and Nam, S.: Rapid decay of slowly moving Typhoon Soulik (2018) due to interactions with the strongly stratified northern East China Sea, Geophysical Research Letters, 46(24), 14595-14603, https://doi.org/10.1029/2019GL086274, 2019.

Phiri, D., Simwanda, M., and Nyirenda, V.: Mapping the impacts of cyclone Idai in Mozambique using Sentinel-2 and OBIA approach, South African Geographical Journal, 103(2), 237-258, https://doi.org/10.1080/03736245.2020.1740104, 2021.

Rodgers, J. C., Murrah, A. W., and Cooke, W. H.: The impact of Hurricane Katrina on the coastal vegetation of the Weeks Bay Reserve, Alabama from NDVI data, Estuaries and

1090   Coasts, 32(3), 496-507, https://doi.org/10.1007/s12237-009-9138-z, 2009.

1091 Rouse, J. W., Haas, J. R. H., Schell, J. A., and Deering, D. W.: Monitoring vegetation systems

1092   in the Great Plains with ERTS, In Proceedings of the 3rd ERTS Symposium,

1093   Washington, DC, USA, 1, 1974.

1094 Ryang, W. H., Kang, S. I., and Cho, K. S.: Characteristics of Surface Topography and

1095   Sediments before and after the Typhoon Soulik in 2018, Macrotidal Coast of Gochang,

1096   Korea, In AGU Fall Meeting Abstracts, OS33B-02, 2021.

1097 Sadik, M., Nakagawa, H., Rahman, M., Shaw, R., Kawaike, K., and Parvin, G. A.: Assessment

1098   of cyclone Aila recovery progress in Bangladesh: a comparison between rice and

1099   shrimp farming villages in Koyra, In Water, Flood Management and Water Security

1100   Under a Changing Climate, Springer, Cham, 109-124, 2020.

1101 Sahoo, B. and Bhaskaran, P. K.: Multi-hazard risk assessment of coastal vulnerability from

1102   tropical cyclones–A GIS based approach for the Odisha coast, Journal of

1103   Environmental Management, 206, 1166-1178, https://doi.org/10.1016/j.jenvman.

1104   2017.10.075, 2018.

1105 Santos, C. A. G., do Nascimento, T. V. M., Mishra, M., and da Silva, R. M.: Analysis of long-

1106   and short-term shoreline change dynamics: A study case of João Pessoa city in Brazil,

1107   Science of the Total Environment, 769, 144889, https://doi.org/10.1016/j.scitotenv.

1108   2020.144889, 2021.

1109 Schneider, A.: Monitoring land cover change in urban and peri-urban areas using dense time

1110   stacks of Landsat satellite data and a data mining approach, Remote Sensing of

1111   Environment, 124, 689-704, https://doi.org/10.1016/j.rse.2012.06.006, 2012.

1112 Shahzad, M. I., Meraj, M., Nazeer, M., Zia, I., Inam, A., Mehmood, K., and Zafar, H.:

1113   Empirical estimation of suspended solids concentration in the Indus Delta Region using

1114   Landsat-7 ETM+ imagery, Journal of Environmental Management, 209, 254-261.,

1115   https://doi.org/10.1016/j.jenvman.2017.12.070, 2018.

1116 Shamsuzzoha, M., Noguchi, R., and Ahamed, T.: Damaged area assessment of cultivated

1117   agricultural lands affected by cyclone bulbul in coastal region of Bangladesh using

1118   Landsat 8 OLI and TIRS datasets, Remote Sensing Applications: Society and

1119   Environment, 23, 100523, https://doi.org/10.1016/j.rsase.2021.100523, 2021.

1120 Sobrino, J. A., Jiménez-Muñoz, J. C., and Paolini, L.: Land surface temperature retrieval from

1121   LANDSAT TM 5, Remote Sensing of Environment, 90(4), 434-440, https://doi.org/

1122   10.1016/j.rse.2004.02.003, 2004.

Son, S., Kim, Y. H., Kwon, J. I., Kim, H. C., and Park, K. S.: Characterization of spatial and temporal variation of suspended sediments in the Yellow and East China Seas using satellite ocean color data, GIScience & Remote Sensing, 51(2), 212-226, https://doi.org/10.1080/15481603.2014.895580, 2014.

Song, W., Mu, X., Ruan, G., Gao, Z., Li, L., and Yan, G.: Estimating fractional vegetation cover and the vegetation index of bare soil and highly dense vegetation with a physically based method, International journal of applied earth observation and geoinformation, 58, 168-176, https://doi.org/10.1016/j.jag.2017.01.015, 2017.

Souza, A. J., Dickey, T. D., and Chang, G. C.: Modeling water column structure and suspended particulate matter on the Middle Atlantic continental shelf during the passages of Hurricanes Edouard and Hortense, Journal of Marine Research, 59(6), 1021-1045, https://doi.org/10.1357/00222400160497751, 2001.

Story, M. and Congalton, R. G.: Accuracy assessment: a user's perspective, Photogrammetric Engineering and Remote Rensing, 52(3), 397-399, 1986.

Tang, R., Shen, F., Ge, J., Yang, S., and Gao, W.: Investigating typhoon impact on SSC through hourly satellite and real-time field observations: A case study of the Yangtze Estuary, Continental Shelf Research, 224, 104475, https://doi.org/10.1016/j.csr.2021.104475, 2021.

Thieler, E. R., Himmelstoss, E. A., Zichichi, J. L., and Ergul, A.: The Digital Shoreline Analysis System (DSAS) version 4.0-an ArcGIS extension for calculating shoreline change (No. 2008-1278), US Geological Survey, 2009.

Tian, Y., Mingming, J., Zongming, W., Dehua, M., Baojia, D., and Chao, W.: Monitoring invasion process of Spartina alterniflora by seasonal Sentinel-2 imagery and an object-based random forest classification, Remote Sensing, 12(9), 1383, https://doi.org/10.3390/rs12091383, 2020.

Tsai, C. H., Tzang, S. Y., Hsiao, S. S., Cheng, C. C., and Li, H. W.: Coastal structure failures and coastal waves on the north coast of Taiwan due to typhoon Herb, Journal of Coastal Research, 22(2), 393-405, 2006.

Tsai, Y. L. S.: Monitoring 23-year of shoreline changes of the Zengwun Estuary in Southern Taiwan using time-series Landsat data and edge detection techniques, Science of The Total Environment, 156310, https://doi.org/10.1016/j.scitotenv.2022.156310, 2022.

Wang, W., Qu, J. J., Hao, X., Liu, Y., and Stanturf, J. A.: Post-hurricane forest damage assessment using satellite remote sensing, Agricultural and forest meteorology, 150(1),

1156   122-132, https://doi.org/10.1016/j.agrformet.2009.09.009, 2010.

1157 Wang, T., Liu, G., Gao, L., Zhu, L., Fu, Q., and Li, D.: Biological and nutrient responses to a
1158   typhoon in the Yangtze Estuary and the adjacent sea, Journal of Coastal Research,
1159   32(2), 323-332, 2016.

1160 Wang, M. and Xu, H.: Remote sensing-based assessment of vegetation damage by a strong
1161   typhoon (Meranti) in Xiamen Island, China, Natural Hazards, 93(3), 1231-1249,
1162   https://doi.org/10.1007/s11069-018-3351-7, 2018.

1163 Wang, S., Mu, L., Qi, M., Yu, Z., Yao, Z., and Zhao, E.: Quantitative risk assessment of storm
1164   surge using GIS techniques and open data: A case study of Daya Bay Zone, China,
1165   Journal of Environmental Management, 289, 112514, https://doi.org/10.1016/j.
1166   jenvman.2021.112514, 2021.

1167 WMO (World Meteorological Organization): Tropical cyclones, Retrieved May 06, 2020 from
1168   https://public.wmo.int/en/our-mandate/focus-areas/natural-hazards-and-disaster-risk-
1169   reduction/tropical-cyclones , 2020.

1170 Wong, M. M. F., Fung, J. C. H., and Yeung, P. P. S.: High-resolution calculation of the urban
1171   vegetation fraction in the Pearl River Delta from the Sentinel-2 NDVI for urban climate
1172   model parameterization, Geoscience Letters, 6(1), 1-10, https://doi.org/
1173   10.1186/s40562-019-0132-4, 2019.

1174 Xu, S., Zhu, X., Helmer, E. H., Tan, X., Tian, J., and Chen, X.: The damage of urban vegetation
1175   from super typhoon is associated with landscape factors: Evidence from Sentinel-2
1176   imagery, International Journal of Applied Earth Observation and Geoinformation, 104,
1177   102536, https://doi.org/10.1016/j.jag.2021.102536, 2021.

1178 Yang, Q., Qin, Z., Li, W., and Xu, B.: Temporal and spatial variations of vegetation cover in
1179   Hulun Buir grassland of Inner Mongolia, China, Arid Land Research and Management,
1180   26(4), 328-343, https://doi.org/10.1080/15324982.2012.709215, 2012.

1181 Yang, Y., Erskine, P. D., Lechner, A. M., Mulligan, D., Zhang, S., and Wang, Z.: Detecting
1182   the dynamics of vegetation disturbance and recovery in surface mining area via Landsat
1183   imagery and LandTrendr algorithm, Journal of Cleaner Production, 178, 353-362,
1184   https://doi.org/10.1016/j.jclepro.2018.01.050, 2018.

1185 Yin, J., Yin, Z., and Xu, S.: Composite risk assessment of typhoon-induced disaster for China's
1186   coastal area, Natural hazards, 69(3), 1423-1434, https://doi.org/10.1007/s11069-013-
1187   0755-2, 2013.

1188 Yoon, W. S., Yoon, S. H., Moon, J. H., and Hong, J. S.: Topographic Variability during

1189   Typhoon Events in Udo Rhodoliths Beach, Jeju Island, South Korea, Ocean and Polar
1190   Research, 43(4), 307-320., 2021.

1191 Yu, J. J., Kim, D., and Yoon, J.: A Study on the Short-term Morphological Beach Changes of
1192   Pado-ri Using UAS-based DEM: Focusing on before and after Typhoon Soulik, Journal
1193   of the Association of Korean Geographers, 7(3), 303-317, 2018.

1194 Yum, S. G., Wei, H. H., and Jang, S. H.: Estimation of the non-exceedance probability of
1195   extreme storm surges in South Korea using tidal-gauge data, Natural Hazards and Earth
1196   System Sciences, 21(8), 2611-2631, https://doi.org/10.5194/nhess-21-2611-2021,
1197   2021.

1198 Zhang, X., Wang, Y., Jiang, H., and Wang, X.: Remote-sensing assessment of forest damage
1199   by Typhoon Saomai and its related factors at landscape scale, International Journal of
1200   Remote Sensing, 34(21), 7874-7886, https://doi.org/10.1080/01431161.2013.827344,
1201   2013.

1202 Zhang, J., Zhang, Z., Chen, J., Chen, H., Jin, J., Han, J., ... and Wei, G.: Estimating soil salinity
1203   with different fractional vegetation cover using remote sensing, Land Degradation &
1204   Development, 32(2), 597-612, https://doi.org/10.1002/ldr.3737, 2021.

1205 Zhang, Y., Sun, Y., Hu, Z., Bian, S., Xiong, C., Liu, J., ... , and Zhang, W.: Increase in
1206   Suspended Sediment Contents by a Storm Surge in Southern Bohai Sea, China,
1207   Mathematical Problems in Engineering, 2022, https://doi.org/10.1155/2022/9585386,
1208   2022.